

Single-Spin Readout and Quantum Sensing using Optomechanically-Induced Transparency

Martin Koppenhöfer¹, Carl Padgett², Jeffrey V. Cady²,

Viraj Dharod², Hyunseok Oh², Ania C. Bleszynski Jayich², and A. A. Clerk¹

¹*Pritzker School of Molecular Engineering, University of Chicago, Chicago, IL 60637, USA*

²*Department of Physics, University of California Santa Barbara, Santa Barbara, CA 93106, USA*

(Dated: December 6, 2022)

Solid-state spin defects are promising quantum sensors for a large variety of sensing targets. Some of these defects couple appreciably to strain in the host material. We propose to use this strain coupling for mechanically-mediated dispersive single-shot spin readout by an optomechanically-induced transparency measurement. Surprisingly, the estimated measurement times for negatively-charged silicon-vacancy defects in diamond are an order of magnitude shorter than those for single-shot optical fluorescence readout.

Introduction— Solid-state defect spins are promising candidates to build powerful quantum sensors [1–4] as well as memories and repeaters for quantum communication [5]. They have a small footprint [6, 7], straightforward operation, and are susceptible to a large variety of sensing targets, such as magnetic [8, 9] and electric fields [10] as well as temperature [11]. Quantum applications (e.g., entanglement-assisted metrology [12–14]) require high-fidelity single-shot spin readout. Optical spin readout is desirable but, unfortunately, not provided by all types of spin defects. Moreover, even many optically addressable spin defects fail to reach robust high-fidelity single-shot readout [5, 15], e.g., because of low photon collection efficiencies, inconvenient optical frequencies, or limited readout times due to non-spin-conserving transitions between orbital ground and excited states.

These issues motivate asking whether other interactions could be harnessed for readout. Recently, it has been shown that some spin defects have an appreciable coupling to strain arising from mechanical vibrations in their host material [16–18]. It has been suggested to use this strain coupling for mechanical cooling [19], mechanical control of the spin defect [16, 20–24], and reservoir engineering [25, 26]. The mechanical mode can also be strongly coupled to electromagnetic modes, e.g., by shaping the host material into an optomechanical crystal (OMC) [27], which enables optical control and fiber-coupled telecom-wavelength optical access, instead of more challenging free-space optical access that is often in the visible range. Diamond OMCs with large optomechanical coupling and integrated nitrogen-vacancy (NV) defects have already been demonstrated experimentally [24, 28, 29].

In this Letter, we show that strain coupling can be used for another crucial functionality: it can enable rapid all-optical dispersive readout of a single solid-state spin, without any orbital excitation. Dispersive readout enables fast, high-fidelity, and quantum-nondemolition (QND) detection in a variety of platforms, including superconducting qubits [30], where the state of the qubit shifts the resonance frequency of a driven microwave cavity and is encoded in the phase of the microwave output

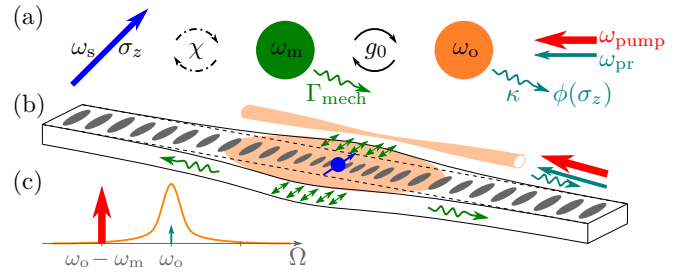


FIG. 1. Dispersive spin readout using optomechanically-induced transparency (OMIT). (a) Sketch of the considered hybrid optomechanical system. A mechanical mode (green circle, center) interacts both with a single spin (blue arrow, left) via a strain-coupling-mediated dispersive interaction, and with an optical mode (orange circle, right) via optomechanical interaction. The optical mode is driven by a pump and a probe laser implementing an OMIT scheme. The σ_z projection of the spin state is encoded in the phase $\phi(\sigma_z)$ of the reflected probe light. All other parameters are defined in the main text. (b) Sketch of a possible experimental implementation using a diamond optomechanical crystal (OMC) with an embedded spin defect (blue) strain-coupled to a mechanical breathing mode (green straight arrows). The optical mode (orange) of the OMC is evanescently coupled to a tapered fiber for optical driving and homodyne detection. (c) Frequencies of the pump and probe lasers. The solid orange curve is the Lorentzian cavity response with width $\kappa < \omega_m$.

field. Using strain coupling, one could try to replicate this by replacing the microwave cavity with a driven, dispersively-coupled mechanical mode. Qubit readout would then require an effective homodyne detection of emitted phonons, which could be done optically using mechanics-to-optics transduction. The scheme we introduce mimics this kind of measurement in a simple and resource-efficient fashion, by exploiting one of the most ubiquitous effects in optomechanics: optomechanically-induced transparency (OMIT) [31–34], where a mechanical mode alters the density-of-states of an optical cavity. While OMIT has been used extensively for device calibration, we show here that, surprisingly, it also paves a powerful route to all-optical single-shot solid-state spin

readout (no explicit mechanical driving or readout is needed). Note that our OMIT-based scheme is distinct from the recently demonstrated optical readout of a superconducting qubit using optomechanical microwave-to-optical transduction [35]. While there are many differences [36], the most crucial is that our scheme has fewer basic ingredients: there is no microwave resonator or drive, nor any microwave-optomechanical coupling.

As a promising experimental example, we analyze readout of a silicon-vacancy (SiV) defect coupled to a diamond OMC. Surprisingly, the estimated spin readout times for realistic experimental parameters [28, 29, 36, 37] are more than a factor of four shorter than the ones for optical cavity-based SiV readout [38], and an order of magnitude shorter than the best optical fluorescence readout times for SiV centers [39] (which are limited by the repolarization timescale of the spin defect into its ground state and require precise alignment of the magnetic field along the SiV axis). In contrast, our dispersive readout is in principle a QND measurement. We stress that our protocol can be applied to other spin-defects (beyond SiV centers) with sufficiently large strain coupling but potentially no optical addressability, since we only assume coupling of an effective two-level system to a mechanical mode.

We also demonstrate that our OMIT-based sensing protocol has applications beyond qubit readout: it can be used for parameter sensing in any optomechanical system where the mechanical frequency depends on an unknown parameter. It exceeds fundamental sensitivity limits that constrain standard schemes employing continuous mechanical position detection [e.g., as used in atomic-force-microscopy (AFM) [40, 41] and mass sensing [42]].

The system— We consider a standard optomechanical (OM) system, sketched in Figs. 1(a,b), with Hamiltonian $\hat{H}_{\text{om}} = \omega_o \hat{a}^\dagger \hat{a} + \omega_m \hat{b}^\dagger \hat{b} - g_0 \hat{a}^\dagger \hat{a} (\hat{b} + \hat{b}^\dagger)$. Here, \hat{a} (\hat{b}) is the annihilation operator of the optical (mechanical) mode with frequency ω_o (ω_m), g_0 is the bare OM coupling strength, and $\hbar = 1$. Both modes interact with dissipative Markovian environments which lead to a decay of optical (mechanical) excitations at a rate κ (Γ_{mech}), with $\kappa \gg \Gamma_{\text{mech}}$. For simplicity, we envisage a several-GHz mechanical mode in a dilution refrigerator, such that thermal occupation is negligible. See [36] for the case of nonzero mechanical temperature.

The mechanical mode is dispersively coupled to a spin, $\hat{H}_{\text{sm}} = \omega_s \hat{\sigma}_z / 2 - \chi \hat{\sigma}_z \hat{b}^\dagger \hat{b}$, where $\hat{\sigma}_z$ is the Pauli z matrix (and commutes with the spin-only Hamiltonian), ω_s is the splitting between the two energy levels, and χ is the dispersive coupling strength. Depending on the σ_z projection of the spin state, the mechanical frequency is shifted by $\varepsilon = -\sigma_z \chi$. In principle, the mechanical frequency shift ε can be measured by driving the mechanical mode with a linear drive and by measuring the phase of the phonons emitted from the mechanical mode into the substrate; this would be a mechanical analogue of a standard cavity QED dispersive readout [30]. Of course,

directly measuring these emitted phonons is infeasible in most setups.

To overcome this issue, we propose an OMIT measurement [31–34], which employs two laser drives as shown in Fig. 1(c). The strong red-detuned pump laser, $\omega_{\text{pump}} = \omega_o - \omega_m$, causes additional mechanical damping and converts part of the dissipated phonons into an optical output field, thus rendering them accessible to conventional optical homodyne detection. Via the OM interaction, it also converts the weak optical probe laser into a linear mechanical drive. Together, these enable all-optical readout of ε , as we now show.

Consider first the situation with only the strong pump laser. It allows us to separate the cavity field into a large semiclassical field amplitude $a \gg 1$ and quantum fluctuations \hat{d} , $\hat{a} = e^{-i\omega_{\text{pump}}t} (a + \hat{d})$, and to linearize the OM interaction [43]. We further assume the good cavity limit $\omega_m \gg \kappa$, allowing us to make a rotating wave approximation on the OM interaction. In a frame rotating at ω_{pump} , the approximate linearized Hamiltonian is:

$$\hat{H} \simeq \omega_m \hat{d}^\dagger \hat{d} + (\omega_m + \varepsilon) \hat{b}^\dagger \hat{b} - G (\hat{b}^\dagger \hat{d} + \hat{b} \hat{d}^\dagger), \quad (1)$$

where $G = g_0 a$ is the optically-enhanced coupling strength. At time $t = 0$ the weak probe laser at frequency ω_{pr} is switched on. We account for this through the cavity input field, $\hat{d}_{\text{in}}(t \geq 0) = a_{\text{pr,in}} e^{-i\omega_m t} + \hat{\xi}_{\text{in}}(t)$, where $\hat{\xi}_{\text{in}}(t)$ is input vacuum noise and $|a_{\text{pr,in}}|^2$ is the photon flux of the probe laser. Note that \hat{d}_{in} describes a probe laser which is resonant with the optical cavity in the lab frame, cf. Fig. 1(c). We also considered a detuned probe laser but found the resonant case to be optimal for qubit readout [36].

Signal-to-noise ratio (SNR)— For $a_{\text{pr,in}} \geq 0$ and $\kappa \gg \Gamma_{\text{mech}}$, the mechanical frequency shift ε is encoded in the $\varphi = \pi/2$ quadrature of the optical output field $\hat{d}_{\text{out}}(t) = \sqrt{\kappa} \hat{d}(t) + \hat{d}_{\text{in}}(t)$ and can be measured by optical homodyne detection. Using the measurement operator describing the integrated homodyne current from $t = 0$ to $t = \tau$,

$$\hat{\mathcal{I}}(\tau) = \sqrt{\kappa} \int_0^\tau dt \left[e^{i\varphi} e^{-i\omega_m t} \hat{d}_{\text{out}}^\dagger(t) + \text{h.c.} \right], \quad (2)$$

the SNR at time τ of our qubit σ_z measurement is defined as [44]

$$\text{SNR}^2(\tau) = \frac{|\langle \hat{\mathcal{I}}(\tau) \rangle_{-\chi} - \langle \hat{\mathcal{I}}(\tau) \rangle_{+\chi}|^2}{\langle [\widehat{\delta \mathcal{I}}(\tau)]^2 \rangle_{-\chi} + \langle [\widehat{\delta \mathcal{I}}(\tau)]^2 \rangle_{+\chi}}, \quad (3)$$

where $\widehat{\delta \mathcal{I}}(\tau) = \hat{\mathcal{I}}(\tau) - \langle \hat{\mathcal{I}}(\tau) \rangle_\varepsilon$ and $\langle \cdot \rangle_\varepsilon$ denotes an expectation value with the mechanical resonance frequency shifted by ε . We focus on the usual limit $G \ll \kappa$ where there is no many-photon OM strong coupling, and where $\chi \ll \kappa$. Note that the effects of χ can still be non-perturbative if $\chi \gtrsim \Gamma_{\text{mech}}$. Using the Heisenberg-Langevin equations for our system [36], we find

$$\text{SNR}^2(\tau) = 8 |a_{\text{pr,in}}|^2 \left(\frac{C_{\text{om}}}{1 + C_{\text{om}}} \right)^2 \sin^2(2\xi)\tau [1 - F(\tau)]^2, \quad (4)$$

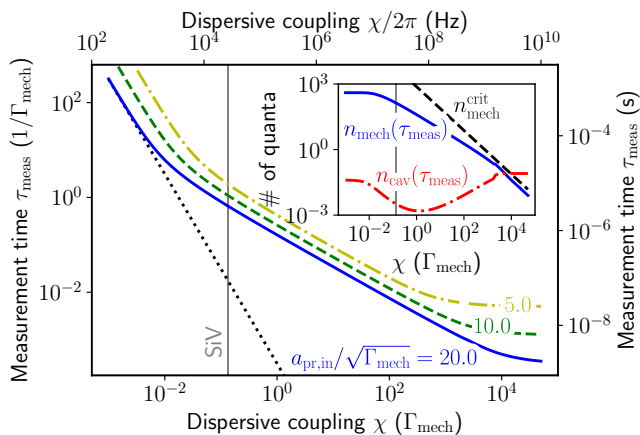


FIG. 2. Minimum measurement time τ_{meas} required to reach a signal-to-noise ratio (SNR) of unity as a function of the spin-mechanical dispersive coupling strength χ . The optomechanical cooperativity C_{om} has been optimized for each data point. The dotted black line indicates the asymptotic form of the measurement time for $\chi/\Gamma_{\text{mech}} \ll 1$ [Eq. (5)]. It ignores transient dynamics and is off by almost two orders of magnitude for the expected parameters for SiV defects in a diamond OMC (gray vertical line). Inset: Phonon number $n_{\text{mech}}(\tau_{\text{meas}})$, photon number $n_{\text{cav}}(\tau_{\text{meas}})$, and critical phonon number $n_{\text{mech}}^{\text{crit}}$ for $a_{\text{pr,in}}/\sqrt{\Gamma_{\text{mech}}} = 20.0$, g_{sm} varied, $\Delta_{\text{sm}}/\Gamma_{\text{mech}} = 750$, and $\kappa/\Gamma_{\text{mech}} = 10000$.

where $F(\tau) = \frac{1}{\chi\tau} [\sin(2\xi) - \sin(2\xi + \chi\tau)e^{-\Gamma_{\text{mech}}(1+C_{\text{om}})\tau/2}]$. The OM cooperativity $C_{\text{om}} = 4G^2/\kappa\Gamma_{\text{mech}}$ can be tuned by varying the pump laser amplitude. As in standard dispersive readout, depending on the frequency shift $\varepsilon = \pm\chi$, $\hat{d}_{\text{out}}(t)$ evolves into one of two different coherent states separated by an angle $2\xi = 2\arctan[2\chi/\Gamma_{\text{mech}}(1+C_{\text{om}})]$. Equation (4) maps to a standard cQED dispersive readout where the cavity damping rate has been replaced by an optically-tunable mechanical damping rate $\Gamma_{\text{mech}}(1+C_{\text{om}})$, and where only a fraction $C_{\text{om}}/(1+C_{\text{om}})$ of the total output flux is detected. As we show, this additional tunability leads to important differences in readout optimization and dynamics.

Measurement time— The measurement time is implicitly defined by $\text{SNR}^2(\tau_{\text{meas}}) = 1$, and our goal is to optimize C_{om} such that τ_{meas} is minimal. As shown in Fig. 2, there are three scalings of τ_{meas} with χ : (i) For a weak strain coupling $\chi \ll \Gamma_{\text{mech}}, \kappa$, the intrinsic mechanical ringup time $1/\Gamma_{\text{mech}}$ will be much shorter than τ_{meas} . The measurement is fastest if the impedance-matching condition $C_{\text{om}} = 1$ holds, in which case

$$\tau_{\text{meas}} \rightarrow \frac{\Gamma_{\text{mech}}^2}{8|a_{\text{pr,in}}|^2\chi^2}. \quad (5)$$

In this regime, the probe laser leads to a steady-state mechanical phonon number $n_{\text{mech}}^{\text{ss}} = \lim_{\tau \rightarrow \infty} n_{\text{mech}}(\tau) = |a_{\text{pr,in}}|^2/\Gamma_{\text{mech}}$ on a timescale shorter than τ_{meas} . (ii) As we show below, spin defects can reach appreciable strain coupling $\chi \gtrsim \Gamma_{\text{mech}}$ such that $\text{SNR}^2(\tau) = 1$ is

achieved before the mechanical steady state is reached. In this regime, is it advantageous to increase C_{om} beyond 1 to speed up the mechanical ring-up, so that this occurs on the same timescale as the measurement (i.e., $C_{\text{om}} \propto 1/\Gamma_{\text{mech}}\tau_{\text{meas}}$). For an optimal C_{om} , we find in this regime $\tau_{\text{meas}} \propto (\chi|a_{\text{pr,in}}|)^{-2/3}$. Reaching the strong-dispersive-coupling regime has been an important goal in cavity QED, circuit QED, and quantum acoustics [45–48]. (iii) Finally, for $\chi \gg \Gamma_{\text{mech}}$, the large detuning $\pm\chi$ between the mechanical mode and the probe laser becomes the limiting factor of the measurement. The optimal cooperativity $C_{\text{om}} = 2\chi/\Gamma_{\text{mech}}$ strongly broadens the mechanical linewidth such that transient dynamics becomes irrelevant again and the measurement time converges to a constant value which depends only on the rate at which probe photons are sent into the system,

$$\tau_{\text{meas}} \rightarrow \frac{1}{8|a_{\text{pr,in}}|^2}. \quad (6)$$

Note that OMIT allows one to optimize the effective damping rate for different values of the dispersive coupling such that one can take advantage of large couplings $\chi \gg \Gamma_{\text{mech}}$.

Critical phonon number— Figure 2 reveals several interesting features. First, τ_{meas} can be smaller than $1/\Gamma_{\text{mech}}$, which reflects the fact that we can broaden the mechanical linewidth optically, $\Gamma_{\text{mech}}(1+C_{\text{om}}) \gg \Gamma_{\text{mech}}$. Second, τ_{meas} is short because we are using many probe phonons. As shown in the inset of Fig. 2, this does not come at the cost of a high photon number (which could cause unwanted heating) since $n_{\text{mech}}^{\text{ss}}/n_{\text{cav}}^{\text{ss}} = \Gamma_{\text{mech}}\kappa C_{\text{om}}/(\Gamma_{\text{mech}}^2 + 4\varepsilon^2) \propto \kappa/\Gamma_{\text{mech}} \gg 1$. Further, with increasing $\chi/\Gamma_{\text{mech}}$, the optimized C_{om} grows and $n_{\text{mech}}^{\text{ss}}$ decreases (as the total mechanical damping is $\propto C_{\text{om}}$). Thanks to the extreme linearity of mechanical modes in OMCs and the small bare optomechanical coupling strength, $n_{\text{mech}}^{\text{ss}} \gg 1$ does not lead to a breakdown of the linearized theory. However, corrections to the dispersive spin-mechanical interaction define a critical phonon number $n_{\text{mech}}^{\text{crit}}$ (see [36]), which limits the maximum probe power, determines the plateau value of τ_{meas} for $\chi \gg \Gamma_{\text{mech}}$, and prevents infinitely fast measurements. Here, we always choose the optical probe power small enough to keep $n_{\text{mech}}^{\text{ss}}$ below the critical phonon number.

Application to SiV systems— Our readout protocol is experimentally feasible with state-of-the-art diamond OMCs and embedded SiV defects. Diamond OMCs with $\kappa/2\pi \approx 2$ GHz have recently been demonstrated by Burek *et al.* [28] and Cady *et al.* [29]. The mechanical modes had $\omega_{\text{m}}/2\pi \approx 6$ GHz and quality factors up to 4100 at room temperature with higher values expected at cryogenic temperatures [28]. A mechanical damping rate $\Gamma_{\text{mech}}/2\pi = 200$ kHz seems thus feasible. The measured optomechanical couplings are $g_0/2\pi \approx 200$ kHz [28, 29]. Spin-mechanical single phonon coupling rates for SiV defects in an OMC have been estimated to be $g_{\text{sm}}/2\pi \approx 2$ MHz [37]. Surprisingly, the strain cou-

pling can be tuned up to $g_{\text{sm}}/2\pi \approx 8$ MHz by applying a suitable off-axis magnetic field without changing the SiV level splitting, as we show in a detailed microscopic analysis in the supplemental material [36]. Using $g_{\text{sm}}/2\pi = 2$ MHz as a conservative estimate and assuming a detuning $\Delta_{\text{sm}} \equiv \omega_{\text{m}} - \omega_{\text{s}} = 2\pi \times 150$ MHz, a dispersive coupling $\chi \equiv g_{\text{sm}}^2/\Delta_{\text{sm}} = 2\pi \times 27$ kHz appears to be realistic. The corresponding ratio $\chi/\Gamma_{\text{mech}} = 0.13$ is indicated by the gray vertical line in Fig. 2.

With these numbers, and using low probe-laser power [such that $n_{\text{mech}}(\tau_{\text{meas}})$ is more than an order of magnitude below $n_{\text{mech}}^{\text{crit}}$, see inset of Fig. 2], we find an estimated measurement time of $\tau_{\text{meas}} = 3.31 \mu\text{s}$. This could be further decreased by using a stronger probe laser. Our τ_{meas} is thus competitive with optical readout times of $13 \mu\text{s}$ for highly strained SiV centers in a diamond nanocavity [38] and $30 \mu\text{s}$ for optical fluorescence readout of SiV centers with an external magnetic field precisely aligned along the SiV axis. In the latter case, the measurement times were limited by the repolarization of the SiV into its ground state on a timescale ≈ 30 ms. For OMIT readout, the estimated measurement times are an order of magnitude shorter, and they will be limited by a Purcell decay time of $\tau_{\text{Purcell}} \approx 28$ ms [36]. We thus find $\tau_{\text{Purcell}}/\tau_{\text{meas}} \approx 8500 \gg 1$, which could be further increased by increasing Δ_{sm} . Given such a large value of $\chi/\Gamma_{\text{mech}}$, one may worry that the spin-mechanical coupling degrades the coherence properties of the SiVs. However, resonant interactions with phonon modes other than the mechanical mode of interest can be suppressed by a suitable design of the OMC. Dephasing of the SiV is irrelevant for spin readout but it may still limit the operation of the SiV as a quantum sensor. Yet, the main phonon-induced dephasing mechanism is dispersive coupling to off-resonant several-GHz phonon modes, which will be highly suppressed at temperatures below 100 mK [36].

Application for quantum sensing— Our OMIT measurement scheme can also be used for more general parameter estimation where the goal is to detect an unknown signal that causes a small mechanical frequency shift $\varepsilon \ll \omega_{\text{m}}$. This basic sensing scheme is widely used, e.g., in atomic-force microscopy (AFM) [40, 41] and mass sensing [42], and it has also been suggested for new OM sensing protocols using limit cycles [49]. Here, with quantum sensing in mind, we are interested in the fundamental limits on the estimation error of such schemes. OMIT allows one to improve the estimation error beyond that of standard schemes using continuous mechanical position detection. Such schemes are fundamentally limited by the standard quantum limit of position detection (SQL-PD) [50, 51]. The estimation error for infinitesimal frequency changes is $(\Delta\varepsilon)^2(\tau) = \lim_{\varepsilon \rightarrow 0} \langle [\delta\hat{\mathcal{I}}(\tau)]^2 \rangle_{\varepsilon} / |\partial_{\varepsilon} \langle \hat{\mathcal{I}}(\tau) \rangle_{\varepsilon}|^2$, which is optimized for a resonant probe laser and $C_{\text{om}} = 1$ [36],

$$(\Delta\varepsilon)^2(\tau) = \frac{\Gamma_{\text{mech}}}{4n_{\text{mech}}^{\text{ss}}\tau} (1 + 2n_{\text{th}} + 2n_{\text{add}}). \quad (7)$$

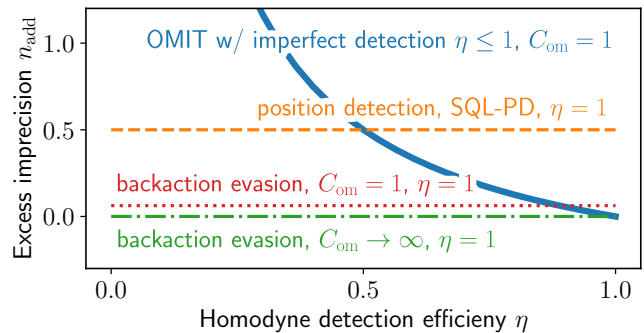


FIG. 3. Comparison of the excess imprecision noise n_{add} [expressed in terms of an equivalent amount of thermal phonons, see Eq. (7)], for sensing a small mechanical frequency shift $\varepsilon \ll \omega_{\text{m}}$ with different measurement schemes. The thick blue line indicates an OMIT measurement with imperfect homodyne detection (efficiency $0 \leq \eta \leq 1$). The thin horizontal lines indicate the smallest excess imprecision noise achievable with other schemes in the limit of perfect homodyne detection, $\eta = 1$.

Here, n_{th} denotes the thermal phonon number due to interaction of the mechanical mode with a finite-temperature environment, and n_{add} represents potential imprecision noise due to the readout of the mechanics, expressed in terms of an equivalent amount of thermal phonons. Note that AFM and limit-cycle sensing protocols yield the same estimation error (7) but are limited by thermal noise, $n_{\text{th}} \gg 1$ and thus typically not sensitive to fundamental imprecision noise [41, 49]. Also note that our goal is not to change the fundamental scaling with $n_{\text{mech}}^{\text{ss}}$, but to make n_{add} as small as possible.

In the ideal case analyzed so far, we have $n_{\text{add}} = 0$ for OMIT readout even when all quantum effects are included. To highlight the significance of this result, it is instructive to compare Eq. (7) with other measurement schemes to determine a small frequency shift ε . Perhaps the most obvious approach is to drive the mechanical resonator linearly at ω_{m} and continuously measure its position $\hat{x} = x_{\text{zpf}}(\hat{b} + \hat{b}^\dagger)$, where x_{zpf} denotes the zero-point fluctuations. This signal can then be used to determine the phase lag between $\langle \hat{x}(t) \rangle$ and the drive (and hence ε). Since this measurement collects information on both quadratures of $\hat{x}(t)$, its estimation error can at best reach the SQL-PD with $n_{\text{add}} = 1/2$ [50, 51].

The SQL-PD can be surpassed by performing a backaction-evading (BAE) measurement [52, 53], which is tuned to measure only the phase quadrature of $\hat{x}(t)$ containing information on ε . In the limit of a large cooperativity $C_{\text{om}} \rightarrow \infty$, one finds $n_{\text{add}} \rightarrow 0$ and thus achieves *the same estimation error* as our OMIT scheme. While BAE measurements (which necessarily require large C_{om}) have been demonstrated [54–58], they are experimentally far more challenging than a simple OMIT measurement with $C_{\text{om}} = 1$ (something that is routinely done for characterization purposes).

The absence of added noise in the OMIT scheme is due to the fact that OMIT (unlike position detection and BAE measurements) transduces both mechanical quadratures into quadratures of the optical output field *without any gain* [36]. By adjusting the local-oscillator phase, one can then choose to measure the optical quadrature $\propto \varepsilon$. Amplification of mechanical quadratures is not required since one can increase the signal by driving the mechanics more strongly, which gives rise to the $1/n_{\text{mech}}^{\text{ss}}$ scaling in Eq. (7). In Fig. 3, we also analyze the case of imperfect homodyne detection (efficiency $0 \leq \eta \leq 1$). In this case, there will be added noise $n_{\text{add}} = (1 - \eta)/2\eta$, but state-of-the-art OMIT detection will surpass the SQL-PD for experimentally feasible efficiencies $\eta \gtrsim 70\%$ [59].

Note that both direct position detection and BAE measurements require careful phase tuning between the mechanical drive and the local oscillator of the homodyne detection. In contrast, our OMIT scheme is an all-optical measurement where the optical probe tone (driving the mechanics) and the local oscillator can be derived from the same laser, eliminating the need for a separate mechanical drive and its phase control.

Conclusion— Our work presents a potentially powerful alternative readout scheme for solid-state spin defects with large strain coupling. This coupling allows one to perform dispersive spin readout using a mechanical mode, which is optically driven and read out using an OMIT scheme. For SiV defects in a diamond OMCs, the estimated readout times are an order of magnitude shorter than the best measurement times for single-shot optical fluorescence readout. Besides spin readout, our scheme is also useful for quantum sensing, when a small signal modifies the resonance frequency of a mechanical oscillator, e.g., strain-mediated readout of the collective

state of a large ensemble of NV centers. As an aside, the closely related phenomenon of optomechanically-induced amplification [34, 60, 61] could also be used for a similar readout scheme when additional signal amplification is needed, e.g., to overcome noise in the post-amplification stage. It would be interesting to check if OMIT readout can also be applied to other types of solid-state spin defects with strain coupling.

Our protocol could be combined with existing ideas to generate remote entanglement between two distant superconducting qubits using dispersive measurements [62, 63]. Recently, strong dispersive coupling between a superconducting qubit and mechanical modes has been used for qubit-based readout of the mechanical state [47, 48], but the mechanical mode was not yet part of an optomechanical system. In addition, conversion of the excitation of a superconducting qubit into an optical photon using piezoelectric coupling to an OMC has been demonstrated [64], but the qubit-mechanical interaction was resonant and only a single red-detuned optical drive had been applied. Our OMIT scheme could be applied to both platforms using small adaptations of the existing setups.

ACKNOWLEDGMENTS

This work was supported by the Defense Advanced Research Projects Agency (DARPA) Driven and Nonequilibrium Quantum Systems (DRINQS) program (Agreement D18AC00014). We also acknowledge support from the DOE Q-NEXT Center (Grant No. DOE 1F-60579), the NSF QLCI program (Grant No. OMA-2016245), and from the Simons Foundation (Grant No. 669487, A. C.). C. P. acknowledges support from the NSF Quantum Foundry at UCSB (NSF DMR-1906325).

-
- [1] V. M. Acosta, E. Bauch, M. P. Ledbetter, C. Santori, K. M. C. Fu, P. E. Barclay, R. G. Beausoleil, H. Linget, J. F. Roch, F. Treussart, S. Chemerisov, W. Gawlik, and D. Budker, Diamonds with a high density of nitrogen-vacancy centers for magnetometry applications, *Phys. Rev. B* **80**, 115202 (2009).
 - [2] S. Steinert, F. Dolde, P. Neumann, A. Aird, B. Naydenov, G. Balasubramanian, F. Jelezko, and J. Wrachtrup, High sensitivity magnetic imaging using an array of spins in diamond, *Review of Scientific Instruments* **81**, 043705 (2010).
 - [3] L. M. Pham, D. L. Sage, P. L. Stanwix, T. K. Yeung, D. Glenn, A. Trifonov, P. Cappellaro, P. R. Hemmer, M. D. Lukin, H. Park, A. Yacoby, and R. L. Walsworth, Magnetic field imaging with nitrogen-vacancy ensembles, *New Journal of Physics* **13**, 045021 (2011).
 - [4] T. Wolf, P. Neumann, K. Nakamura, H. Sumiya, T. Ohshima, J. Isoya, and J. Wrachtrup, Subpicotesla diamond magnetometry, *Phys. Rev. X* **5**, 041001 (2015).
 - [5] D. D. Awschalom, R. Hanson, J. Wrachtrup, and B. B. Zhou, Quantum technologies with optically interfaced solid-state spins, *Nature Photonics* **12**, 516 (2018).
 - [6] H. J. Mamin, M. Kim, M. H. Sherwood, C. T. Rettner, K. Ohno, D. D. Awschalom, and D. Rugar, Nanoscale nuclear magnetic resonance with a nitrogen-vacancy spin sensor, *Science* **339**, 557 (2013).
 - [7] T. Staudacher, F. Shi, S. Pezzagna, J. Meijer, J. Du, C. A. Meriles, F. Reinhard, and J. Wrachtrup, Nuclear magnetic resonance spectroscopy on a (5-nanometer)³ sample volume, *Science* **339**, 561 (2013).
 - [8] J. M. Taylor, P. Cappellaro, L. Childress, L. Jiang, D. Budker, P. R. Hemmer, A. Yacoby, R. Walsworth, and M. D. Lukin, High-sensitivity diamond magnetometer with nanoscale resolution, *Nature Physics* **4**, 810 (2008).
 - [9] L. Rondin, J.-P. Tetienne, T. Hingant, J.-F. Roch, P. Maletinsky, and V. Jacques, Magnetometry with nitrogen-vacancy defects in diamond, *Reports on Progress in Physics* **77**, 056503 (2014).
 - [10] F. Dolde, H. Fedder, M. W. Doherty, T. Nöbauer, F. Rempp, G. Balasubramanian, T. Wolf, F. Reinhard, L. C. L. Hollenberg, F. Jelezko, and J. Wrachtrup, Electric-field sensing using single diamond spins, *Nature*

- Physics* **7**, 459 (2011).
- [11] V. M. Acosta, E. Bauch, M. P. Ledbetter, A. Waxman, L.-S. Bouchard, and D. Budker, Temperature dependence of the nitrogen-vacancy magnetic resonance in diamond, *Phys. Rev. Lett.* **104**, 070801 (2010).
- [12] V. Giovannetti, S. Lloyd, and L. Maccone, Quantum-enhanced measurements: Beating the standard quantum limit, *Science* **306**, 1330 (2004).
- [13] C. L. Degen, F. Reinhard, and P. Cappellaro, Quantum sensing, *Rev. Mod. Phys.* **89**, 035002 (2017).
- [14] L. Pezzè, A. Smerzi, M. K. Oberthaler, R. Schmied, and P. Treutlein, Quantum metrology with nonclassical states of atomic ensembles, *Rev. Mod. Phys.* **90**, 035005 (2018).
- [15] J. F. Barry, J. M. Schloss, E. Bauch, M. J. Turner, C. A. Hart, L. M. Pham, and R. L. Walsworth, Sensitivity optimization for NV-diamond magnetometry, *Rev. Mod. Phys.* **92**, 015004 (2020).
- [16] S. Meesala, Y.-I. Sohn, H. A. Atikian, S. Kim, M. J. Burek, J. T. Choy, and M. Lončar, Enhanced strain coupling of nitrogen-vacancy spins to nanoscale diamond cantilevers, *Phys. Rev. Applied* **5**, 034010 (2016).
- [17] D. Lee, K. W. Lee, J. V. Cady, P. Ovarthaiyapong, and A. C. B. Jayich, Topical review: spins and mechanics in diamond, *Journal of Optics* **19**, 033001 (2017).
- [18] S. Meesala, Y.-I. Sohn, B. Pingault, L. Shao, H. A. Atikian, J. Holzgrafe, M. Gündogan, C. Stavrakas, A. Sipahigil, C. Chia, R. Evans, M. J. Burek, M. Zhang, L. Wu, J. L. Pacheco, J. Abraham, E. Bielejec, M. D. Lukin, M. Atatüre, and M. Lončar, Strain engineering of the silicon-vacancy center in diamond, *Phys. Rev. B* **97**, 205444 (2018).
- [19] K. V. Kepesidis, M.-A. Lemonde, A. Norambuena, J. R. Maze, and P. Rabl, Cooling phonons with phonons: Acoustic reservoir engineering with silicon-vacancy centers in diamond, *Phys. Rev. B* **94**, 214115 (2016).
- [20] E. R. MacQuarrie, T. A. Gosavi, N. R. Jungwirth, S. A. Bhave, and G. D. Fuchs, Mechanical spin control of nitrogen-vacancy centers in diamond, *Phys. Rev. Lett.* **111**, 227602 (2013).
- [21] E. R. MacQuarrie, T. A. Gosavi, A. M. Moehle, N. R. Jungwirth, S. A. Bhave, and G. D. Fuchs, Coherent control of a nitrogen-vacancy center spin ensemble with a diamond mechanical resonator, *Optica* **2**, 233 (2015).
- [22] A. Barfuss, J. Teissier, E. Neu, A. Nunnenkamp, and P. Maletinsky, Strong mechanical driving of a single electron spin, *Nature Physics* **11**, 820 (2015).
- [23] K. W. Lee, D. Lee, P. Ovarthaiyapong, J. Minguzzi, J. R. Maze, and A. C. Bleszynski Jayich, Strain coupling of a mechanical resonator to a single quantum emitter in diamond, *Phys. Rev. Applied* **6**, 034005 (2016).
- [24] D. A. Golter, T. Oo, M. Amezcua, K. A. Stewart, and H. Wang, Optomechanical quantum control of a nitrogen-vacancy center in diamond, *Phys. Rev. Lett.* **116**, 143602 (2016).
- [25] P. Groszkowski, M. Koppenhöfer, H.-K. Lau, and A. A. Clerk, Reservoir-engineered spin squeezing: Macroscopic even-odd effects and hybrid-systems implementations, *Phys. Rev. X* **12**, 011015 (2022).
- [26] J. M. Kitzman, J. R. Lane, C. Undershute, P. M. Harrington, N. R. Beysengulov, C. A. Mikolas, K. W. Murch, and J. Pollanen, Quantum acoustic bath engineering, *arXiv* , 2208.07423v1 (2022).
- [27] M. Eichenfield, J. Chan, R. M. Camacho, K. J. Vahala, and O. Painter, Optomechanical crystals, *Nature* **462**, 78 (2009).
- [28] M. J. Burek, J. D. Cohen, S. M. Meenehan, N. El-Sawah, C. Chia, T. Ruelle, S. Meesala, J. Rochman, H. A. Atikian, M. Markham, D. J. Twitchen, M. D. Lukin, O. Painter, and M. Lončar, Diamond optomechanical crystals, *Optica* **3**, 1404 (2016).
- [29] J. V. Cady, O. Michel, K. W. Lee, R. N. Patel, C. J. Sarabalis, A. H. Safavi-Naeini, and A. C. B. Jayich, Diamond optomechanical crystals with embedded nitrogen-vacancy centers, *Quantum Science and Technology* **4**, 024009 (2019).
- [30] A. Blais, A. L. Grimsmo, S. M. Girvin, and A. Wallraff, Circuit quantum electrodynamics, *Rev. Mod. Phys.* **93**, 025005 (2021).
- [31] A. Schliesser, *Cavity optomechanics and optical frequency comb generation with silica whispering-gallery-mode resonators*, Ph.D. thesis, Ludwig-Maximilians-Universität München (2009).
- [32] G. S. Agarwal and S. Huang, Electromagnetically induced transparency in mechanical effects of light, *Phys. Rev. A* **81**, 041803 (2010).
- [33] S. Weis, R. Rivière, S. Deléglise, E. Gavartin, O. Arcizet, A. Schliesser, and T. J. Kippenberg, Optomechanically induced transparency, *Science* **330**, 1520 (2010).
- [34] A. H. Safavi-Naeini, T. P. M. Alegre, J. Chan, M. Eichenfield, M. Winger, Q. Lin, J. T. Hill, D. E. Chang, and O. Painter, Electromagnetically induced transparency and slow light with optomechanics, *Nature* **472**, 69 (2011).
- [35] R. D. Delaney, M. D. Urmey, S. Mittal, B. M. Brubaker, J. M. Kindem, P. S. Burns, C. A. Regal, and K. W. Lehnert, Superconducting-qubit readout via low-backaction electro-optic transduction, *Nature* **606**, 489 (2022).
- [36] See supplemental material at [url will be inserted by publisher] for additional details on the omit readout protocol, which includes refs. [65–70].
- [37] P. K. Shandilya, D. P. Lake, M. J. Mitchell, D. D. Sukachev, and P. E. Barclay, Optomechanical interface between telecom photons and spin quantum memory, *Nature Physics* **17**, 1420 (2021).
- [38] C. T. Nguyen, D. D. Sukachev, M. K. Bhaskar, B. Machielse, D. S. Levonian, E. N. Knall, P. Stroganov, R. Riedinger, H. Park, M. Lončar, and M. D. Lukin, Quantum network nodes based on diamond qubits with an efficient nanophotonic interface, *Phys. Rev. Lett.* **123**, 183602 (2019).
- [39] D. D. Sukachev, A. Sipahigil, C. T. Nguyen, M. K. Bhaskar, R. E. Evans, F. Jelezko, and M. D. Lukin, Silicon-vacancy spin qubit in diamond: A quantum memory exceeding 10 ms with single-shot state readout, *Phys. Rev. Lett.* **119**, 223602 (2017).
- [40] Y. Martin, C. C. Williams, and H. K. Wickramasinghe, Atomic force microscope–force mapping and profiling on a sub 100-Å scale, *Journal of Applied Physics* **61**, 4723 (1987).
- [41] T. R. Albrecht, P. Grütter, D. Horne, and D. Rugar, Frequency modulation detection using high-Q cantilevers for enhanced force microscope sensitivity, *Journal of Applied Physics* **69**, 668 (1991).
- [42] K. L. Ekinci, Y. T. Yang, and M. L. Roukes, Ultimate limits to inertial mass sensing based upon nanoelectromechanical systems, *Journal of Applied Physics* **95**, 2682 (2004).
- [43] M. Aspelmeyer, T. J. Kippenberg, and F. Marquardt,

- Cavity optomechanics, *Rev. Mod. Phys.* **86**, 1391 (2014).
- [44] N. Didier, A. Kamal, W. D. Oliver, A. Blais, and A. A. Clerk, Heisenberg-limited qubit read-out with two-mode squeezed light, *Phys. Rev. Lett.* **115**, 093604 (2015).
- [45] P. Bertet, A. Auffeves, P. Maioli, S. Osnaghi, T. Meunier, M. Brune, J. M. Raimond, and S. Haroche, Direct measurement of the Wigner function of a one-photon fock state in a cavity, *Phys. Rev. Lett.* **89**, 200402 (2002).
- [46] A. Wallraff, D. I. Schuster, A. Blais, L. Frunzio, R. S. Huang, J. Majer, S. Kumar, S. M. Girvin, and R. J. Schoelkopf, Strong coupling of a single photon to a superconducting qubit using circuit quantum electrodynamics, *Nature* **431**, 162 (2004).
- [47] U. von Lüpke, Y. Yang, M. Bild, L. Michaud, M. Fadel, and Y. Chu, Parity measurement in the strong dispersive regime of circuit quantum acoustodynamics, *Nature Physics* **18**, 794 (2022).
- [48] E. A. Wollack, A. Y. Cleland, R. G. Gruenke, Z. Wang, P. Arrangoiz-Arriola, and A. H. Safavi-Naeini, Quantum state preparation and tomography of entangled mechanical resonators, *Nature* **604**, 463 (2022).
- [49] B. Guha, P. E. Allain, A. Lemaître, G. Leo, and I. Favero, Force sensing with an optomechanical self-oscillator, *Phys. Rev. Applied* **14**, 024079 (2020).
- [50] V. B. Braginsky and F. Y. Khalili, *Quantum measurement*, edited by K. S. Thorne (Cambridge University Press, 1992).
- [51] A. A. Clerk, M. H. Devoret, S. M. Girvin, F. Marquardt, and R. J. Schoelkopf, Introduction to quantum noise, measurement, and amplification, *Rev. Mod. Phys.* **82**, 1155 (2010).
- [52] V. B. Braginsky, Y. I. Vorontsov, and K. S. Thorne, Quantum nondemolition measurements, *Science* **209**, 547 (1980).
- [53] A. A. Clerk, F. Marquardt, and K. Jacobs, Back-action evasion and squeezing of a mechanical resonator using a cavity detector, *New Journal of Physics* **10**, 095010 (2008).
- [54] J. B. Hertzberg, T. Rocheleau, T. Ndukum, M. Savva, A. A. Clerk, and K. C. Schwab, Back-action-evading measurements of nanomechanical motion, *Nature Physics* **6**, 213 (2010).
- [55] J. Suh, A. J. Weinstein, C. U. Lei, E. E. Wollman, S. K. Steinke, P. Meystre, A. A. Clerk, and K. C. Schwab, Mechanically detecting and avoiding the quantum fluctuations of a microwave field, *Science* **344**, 1262 (2014).
- [56] F. Lecocq, J. B. Clark, R. W. Simmonds, J. Aumentado, and J. D. Teufel, Quantum nondemolition measurement of a nonclassical state of a massive object, *Phys. Rev. X* **5**, 041037 (2015).
- [57] C. F. Ockeloen-Korppi, E. Damskägg, J.-M. Pirkkalainen, A. A. Clerk, M. J. Woolley, and M. A. Sillanpää, Quantum backaction evading measurement of collective mechanical modes, *Phys. Rev. Lett.* **117**, 140401 (2016).
- [58] I. Shomroni, L. Qiu, D. Malz, A. Nunnenkamp, and T. J. Kippenberg, Optical backaction-evading measurement of a mechanical oscillator, *Nature Communications* **10**, 2086 (2019).
- [59] T. P. Purdy, P.-L. Yu, R. W. Peterson, N. S. Kampel, and C. A. Regal, Strong optomechanical squeezing of light, *Phys. Rev. X* **3**, 031012 (2013).
- [60] F. Massel, T. T. Heikkilä, J.-M. Pirkkalainen, S. U. Cho, H. Saloniemi, P. J. Hakonen, and M. A. Sillanpää, Microwave amplification with nanomechanical resonators, *Nature* **480**, 351 (2011).
- [61] F. Hocke, X. Zhou, A. Schliesser, T. J. Kippenberg, H. Huebl, and R. Gross, Electromechanically induced absorption in a circuit nano-electromechanical system, *New Journal of Physics* **14**, 123037 (2012).
- [62] N. Roch, M. E. Schwartz, F. Motzoi, C. Macklin, R. Vijay, A. W. Eddins, A. N. Korotkov, K. B. Whaley, M. Sarovar, and I. Siddiqi, Observation of measurement-induced entanglement and quantum trajectories of remote superconducting qubits, *Phys. Rev. Lett.* **112**, 170501 (2014).
- [63] M. Silveri, E. Zaly-Geller, M. Hatridge, Z. Leghtas, M. H. Devoret, and S. M. Girvin, Theory of remote entanglement via quantum-limited phase-preserving amplification, *Phys. Rev. A* **93**, 062310 (2016).
- [64] M. Mirhosseini, A. Sipahigil, M. Kalaei, and O. Painter, Superconducting qubit to optical photon transduction, *Nature* **588**, 599 (2020).
- [65] M. Aspelmeyer, T. J. Kippenberg, and F. Marquardt, eds., *Cavity Optomechanics* (Springer Berlin, Heidelberg, 2014).
- [66] M.-A. Lemonde, N. Didier, and A. A. Clerk, Nonlinear interaction effects in a strongly driven optomechanical cavity, *Phys. Rev. Lett.* **111**, 053602 (2013).
- [67] C. Hepp, *Electronic structure of the silicon vacancy color center in diamond*, Ph.D. thesis, Universität des Saarlandes (2014).
- [68] A. Gali and J. R. Maze, Ab initio study of the split silicon-vacancy defect in diamond: Electronic structure and related properties, *Phys. Rev. B* **88**, 235205 (2013).
- [69] C. Hepp, T. Müller, V. Waselowski, J. N. Becker, B. Pingault, H. Sternschulte, D. Steinmüller-Nethl, A. Gali, J. R. Maze, M. Atatüre, and C. Becher, Electronic structure of the silicon vacancy color center in diamond, *Phys. Rev. Lett.* **112**, 036405 (2014).
- [70] C. M. Caves, Quantum limits on noise in linear amplifiers, *Phys. Rev. D* **26**, 1817 (1982).

Supplemental Material for Single-Spin Readout and Quantum Sensing using Optomechanically-Induced Transparency

Martin Koppenhöfer¹, Carl Padgett², Jeffrey V. Cady²,
Viraj Dharod², Hyunseok Oh², Ania C. Bleszynski Jayich², and A. A. Clerk¹
¹*Pritzker School of Molecular Engineering, University of Chicago, Chicago, IL 60637, USA*
²*Department of Physics, University of California Santa Barbara, Santa Barbara, CA 93106, USA*
(Dated: December 6, 2022)

CONTENTS

I. Optical and mechanical output fields	1
II. Signal-to-noise ratio for dispersive readout	3
III. Critical phonon number	5
IV. Finite-temperature case	6
V. Bounded optomechanical cooperativity	7
VI. Estimated strain coupling for SiV defects	8
VII. Quantum sensing using OMIT	11
A. Estimation error	11
B. Comparison of different detection schemes	11
C. Impact of imperfect homodyne detection	14
VIII. Difference to optical superconducting qubit readout using microwave-to-optical transduction	14

I. OPTICAL AND MECHANICAL OUTPUT FIELDS

We consider an optomechanical system with an optical mode \hat{a} (at frequency ω_o) and a mechanical mode \hat{b} (at frequency ω_m), which are coupled with a bare optomechanical coupling strength g_0 ,

$$\hat{H}_{\text{om}} = \omega_o \hat{a}^\dagger \hat{a} + \omega_m \hat{b}^\dagger \hat{b} - g_0 \hat{a}^\dagger \hat{a} (\hat{b}^\dagger + \hat{b}) . \quad (\text{S1})$$

Here and in the following, we set $\hbar = 1$. The optical mode is driven by a strong pump laser at frequency $\omega_{\text{pump}} = \omega_o - \omega_m$,

$$\hat{H}_{\text{pump}} = \sqrt{\kappa} [a_{\text{pump,in}}(t) \hat{a}^\dagger + a_{\text{pump,in}}^*(t) \hat{a}] , \quad (\text{S2})$$

where $a_{\text{pump,in}}(t) = \bar{a}_{\text{pump,in}} e^{-i\omega_{\text{pump}} t}$ is the semiclassical part of the input field due to the pump laser and κ is the decay rate of the optical mode due to coupling to the input/output channel. The photon flux of the pump laser is given by $|\bar{a}_{\text{pump,in}}|^2$. The mechanical mode is coupled to a single spin-1/2 system (with level-splitting energy ω_s) by a Jaynes-Cummings interaction with spin-mechanical coupling strength g_{sm} ,

$$\hat{H}_{\text{JC}} = \frac{\omega_s}{2} \hat{\sigma}_z + g_{\text{sm}} (\hat{\sigma}_+ \hat{b} + \hat{\sigma}_- \hat{b}^\dagger) . \quad (\text{S3})$$

Here, $\hat{\sigma}_{x,y,z}$ are the Pauli matrices, and $\hat{\sigma}_\pm = (\hat{\sigma}_x \pm i\hat{\sigma}_y)/2$ are the spin raising and lowering operators, respectively. Both the optical and the mechanical mode are coupled to a dissipative environment modeled by a Lindblad quantum master equation,

$$\frac{d}{dt} \hat{\rho} = -i [\hat{H}_{\text{om}} + \hat{H}_{\text{JC}} + \hat{H}_{\text{pump}}, \hat{\rho}] + \kappa \mathcal{D}[\hat{a}] \hat{\rho} + \Gamma_{\text{mech}} (n_{\text{th}} + 1) \mathcal{D}[\hat{b}] \hat{\rho} + \Gamma_{\text{mech}} n_{\text{th}} \mathcal{D}[\hat{b}^\dagger] \hat{\rho} , \quad (\text{S4})$$

where Γ_{mech} is the bare mechanical decay rate, n_{th} is the thermal phonon number, and the Lindblad dissipators are defined as $\mathcal{D}[\hat{O}]\hat{\rho} = \hat{O}\hat{\rho}\hat{O}^\dagger - \{\hat{O}^\dagger\hat{O}, \hat{\rho}\}/2$. We assume that the spins are strongly detuned from the mechanical mode, $|\Delta_{\text{sm}}| \equiv |\omega_{\text{m}} - \omega_{\text{s}}| \gg g_{\text{sm}}$, such that the spin-mechanical interaction can be diagonalized up to second order in $g_{\text{sm}}/\Delta_{\text{sm}}$ by a Schrieffer-Wolff transformation $\hat{H}' = e^{\hat{S}}\hat{H}e^{-\hat{S}}$ with

$$\hat{S} = \frac{g_{\text{sm}}}{\Delta_{\text{sm}}} \left(\hat{b}^\dagger \hat{\sigma}_- - \hat{b} \hat{\sigma}_+ \right). \quad (\text{S5})$$

The resulting dynamics is

$$\begin{aligned} \frac{d}{dt}\hat{\rho} = & -i \left[\hat{H}_{\text{om}} + \hat{H}'_{\text{JC}} + \hat{H}_{\text{pump}} + \hat{H}'_{\text{so}}, \hat{\rho} \right] \\ & + \kappa \mathcal{D}[\hat{a}]\hat{\rho} + \Gamma_{\text{mech}}(n_{\text{th}} + 1)\mathcal{D}[\hat{b}]\hat{\rho} + \Gamma_{\text{mech}}n_{\text{th}}\mathcal{D}[\hat{b}^\dagger]\hat{\rho} + \frac{\Gamma_{\text{mech}}\chi}{\Delta_{\text{sm}}}(n_{\text{th}} + 1)\mathcal{D}[\hat{\sigma}_-]\hat{\rho} + \frac{\Gamma_{\text{mech}}\chi}{\Delta_{\text{sm}}}n_{\text{th}}\mathcal{D}[\hat{\sigma}_+]\hat{\rho}, \end{aligned} \quad (\text{S6})$$

$$\hat{H}'_{\text{JC}} = \frac{\omega_{\text{s}}}{2}\hat{\sigma}_z - \frac{\chi}{2}(1 + \hat{\sigma}_z) - \chi\hat{\sigma}_z\hat{b}^\dagger\hat{b}, \quad (\text{S7})$$

$$\hat{H}'_{\text{so}} = \frac{g_0\chi}{g_{\text{sm}}}\hat{a}^\dagger\hat{a}(\hat{\sigma}_- + \hat{\sigma}_+), \quad (\text{S8})$$

where we introduced the dispersive coupling strength $\chi = g_{\text{sm}}^2/\Delta_{\text{sm}}$. For typical experimental parameters, the condition $\chi \ll \omega_{\text{s}}$ holds and we can neglect the correction to the spin-transition frequency, $\omega_{\text{s}} - \chi \approx \omega_{\text{s}}$. Ignoring the constant shift $-\chi/2$, we thus find the spin-mechanical interaction Hamiltonian given in the main text, $\hat{H}'_{\text{JC}} \approx \hat{H}_{\text{sm}} = \omega_{\text{s}}\hat{\sigma}_z/2 - \chi\hat{\sigma}_z\hat{b}^\dagger\hat{b}$.

To simplify the optomechanical Hamiltonian, we switch to a rotating frame at the pump laser frequency ω_{pump} , decompose the optical field into a large semiclassical amplitude a due to the pump laser and quantum fluctuations \hat{d} around it,

$$\hat{a} = e^{-i\omega_{\text{pump}}t} \left(a + \hat{d} \right), \quad (\text{S9})$$

and linearize the optomechanical interaction [43]. Assuming a to be real without loss of generality, we obtain

$$\begin{aligned} \frac{d}{dt}\hat{\rho} = & -i \left[\hat{H}'_{\text{om}} + \hat{H}_{\text{sm}}, \hat{\rho} \right] + \kappa \mathcal{D}[\hat{d}]\hat{\rho} + \Gamma_{\text{mech}}(n_{\text{th}} + 1)\mathcal{D}[\hat{b}]\hat{\rho} + \Gamma_{\text{mech}}n_{\text{th}}\mathcal{D}[\hat{b}^\dagger]\hat{\rho} \\ & + \frac{\Gamma_{\text{mech}}\chi}{\Delta_{\text{sm}}}(n_{\text{th}} + 1)\mathcal{D}[\hat{\sigma}_-]\hat{\rho} + \frac{\Gamma_{\text{mech}}\chi}{\Delta_{\text{sm}}}n_{\text{th}}\mathcal{D}[\hat{\sigma}_+]\hat{\rho}, \end{aligned} \quad (\text{S10})$$

$$\hat{H}'_{\text{om}} = -\Delta_{\text{opt}}\hat{d}^\dagger\hat{d} + \omega_{\text{m}}\hat{b}^\dagger\hat{b} - G \left(\hat{b}\hat{d}^\dagger + \hat{b}^\dagger\hat{d} \right), \quad (\text{S11})$$

where we introduced the detuning $\Delta_{\text{opt}} = \omega_{\text{pump}} - \omega_{\text{o}}$ and the optically-enhanced coupling strength $G = g_0a$. The direct spin-optical interaction term \hat{H}'_{so} contains only fast rotating terms and can be ignored if the condition $G\chi/g_{\text{sm}} \ll |\Delta_{\text{sm}}|$ holds, which is well satisfied for typical experimental parameters. The linearized optomechanical Hamiltonian \hat{H} given in Eq. (1) of the main text is \hat{H}'_{om} with $\Delta_{\text{opt}} = -\omega_{\text{m}}$ including the dispersive frequency shift $\varepsilon = -\chi\langle\hat{\sigma}_z\rangle$ stemming from the spin-mechanical interaction term in \hat{H}_{sm} .

From Eq. (S10), we obtain the following Heisenberg-Langevin equations of motion for the mechanical mode \hat{b} and the optical fluctuations \hat{d} .

$$\frac{d}{dt}\hat{d} = - \left[\frac{\kappa}{2} - i\Delta_{\text{opt}} \right] \hat{d} + iG\hat{b} - \sqrt{\kappa}\hat{d}_{\text{in}}, \quad (\text{S12})$$

$$\frac{d}{dt}\hat{b} = - \left[\frac{\Gamma_{\text{mech}}}{2} + i(\omega_{\text{m}} + \varepsilon) \right] \hat{b} + iG\hat{d} - \sqrt{\Gamma_{\text{mech}}}\hat{b}_{\text{in}}, \quad (\text{S13})$$

where \hat{d}_{in} and \hat{b}_{in} are the optical and mechanical input fields, respectively, and $\varepsilon = -\chi\langle\hat{\sigma}_z\rangle$ is a spin-state-dependent mechanical frequency shift. Note that, apart from the Purcell decay terms in Eq. (S10), $\hat{\sigma}_z$ is a constant of motion. The Purcell decay times $\tau_{\text{Purcell}} \propto \Delta_{\text{sm}}/\Gamma_{\text{mech}}\chi$ can be made arbitrarily large by increasing the spin-mechanical detuning Δ_{sm} , such that we implement a quantum-nondemolition (QND) measurement. The optical input field contains the semiclassical field of the weak probe laser (which is switched on instantaneously at $t = 0$) as well as zero-temperature Gaussian white noise $\hat{\xi}_{\text{in}}$,

$$\hat{d}_{\text{in}}(t) = a_{\text{pr,in}}e^{-i\tilde{\omega}_{\text{pr}}t}\Theta(t) + \hat{\xi}_{\text{in}}(t), \quad (\text{S14})$$

$$\langle \hat{\xi}_{\text{in}}(t)\hat{\xi}_{\text{in}}^\dagger(t') \rangle = \delta(t - t'), \quad (\text{S15})$$

where $\Theta(t)$ denotes the Heaviside step function and $|a_{\text{pr, in}}|^2$ is the photon flux due to the probe laser. Note that \hat{d} and \hat{d}_{in} are defined in a frame rotating at ω_{pump} , i.e., the probe frequency in the lab frame is given by $\omega_{\text{pr}} = \omega_{\text{pump}} + \tilde{\omega}_{\text{pr}} = \omega_{\text{o}} - \omega_{\text{m}} + \tilde{\omega}_{\text{pr}}$ and the probe laser is on resonance with the optical cavity if $\tilde{\omega}_{\text{pr}} = \omega_{\text{m}}$. The mechanical input field is given by finite-temperature Gaussian white noise,

$$\langle \hat{b}_{\text{in}}(t) \hat{b}_{\text{in}}^\dagger(t') \rangle = (n_{\text{th}} + 1) \delta(t - t'), \quad (\text{S16})$$

$$\langle \hat{b}_{\text{in}}^\dagger(t) \hat{b}_{\text{in}}(t') \rangle = n_{\text{th}} \delta(t - t'). \quad (\text{S17})$$

The Heisenberg-Langevin equations (S12) and (S13) can be solved exactly,

$$\begin{pmatrix} \hat{d}(t) \\ \hat{b}(t) \end{pmatrix} = - \int_{-\infty}^{\infty} dt' \mathcal{G}(t - t') \cdot \begin{pmatrix} \sqrt{\kappa} & 0 \\ 0 & \sqrt{\Gamma_{\text{mech}}} \end{pmatrix} \cdot \begin{pmatrix} \hat{d}_{\text{in}}(t') \\ \hat{b}_{\text{in}}(t') \end{pmatrix}, \quad (\text{S18})$$

where $\mathcal{G}(\tau)$ denotes the Green's function of the Heisenberg-Langevin equations,

$$\begin{aligned} \mathcal{G}(\tau) &= \Theta(\tau) e^{-i\tau(\omega_{\text{m}} + \varepsilon/2) - (\Gamma_{\text{mech}} + \kappa)\tau/4} \begin{pmatrix} G_{dd}(\tau) & G_{db}(\tau) \\ G_{bd}(\tau) & G_{bb}(\tau) \end{pmatrix}, \\ G_{dd}(\tau) &= \cosh \left[\frac{\tau \sqrt{\dots}}{4} \right] + \frac{\Gamma_{\text{mech}} - \kappa + 2i\varepsilon}{\sqrt{\dots}} \sinh \left[\frac{\tau \sqrt{\dots}}{4} \right], \\ G_{bb}(\tau) &= \cosh \left[\frac{\tau \sqrt{\dots}}{4} \right] - \frac{\Gamma_{\text{mech}} - \kappa + 2i\varepsilon}{\sqrt{\dots}} \sinh \left[\frac{\tau \sqrt{\dots}}{4} \right], \\ G_{db}(\tau) &= G_{bd}(\tau) = \frac{2i\sqrt{C_{\text{om}}\Gamma_{\text{mech}}\kappa}}{\sqrt{\dots}} \sinh \left[\frac{\tau \sqrt{\dots}}{4} \right], \end{aligned} \quad (\text{S19})$$

Here, we introduced the optomechanical cooperativity $C_{\text{om}} = 4G^2/\kappa\Gamma_{\text{mech}}$ and the abbreviation $\sqrt{\dots} = \sqrt{\Gamma_{\text{mech}}^2 - (2\varepsilon + i\kappa)^2 - 2\Gamma_{\text{mech}}[-2i\varepsilon + \kappa(1 + 2C_{\text{om}})]}$. From this result, we can calculate the optical and mechanical output fields using standard input-output theory

$$\hat{d}_{\text{out}}(t) = \sqrt{\kappa} \hat{d}(t) + \hat{d}_{\text{in}}(t), \quad (\text{S20})$$

$$\hat{b}_{\text{out}}(t) = \sqrt{\Gamma_{\text{mech}}} \hat{b}(t) + \hat{b}_{\text{in}}(t). \quad (\text{S21})$$

II. SIGNAL-TO-NOISE RATIO FOR DISPERSIVE READOUT

The information on the spin's σ_z projection is encoded in the phase shift of the optical output field at the frequency of the probe laser. It can be read out by homodyne detection of a suitable quadrature of the optical output field, and integrating the output signal for a time τ . Such a measurement is described by the observable

$$\hat{\mathcal{I}}(\tau) = \sqrt{\kappa} \int_0^\tau dt \left[e^{i\varphi} e^{-i\tilde{\omega}_{\text{pr}}t} \hat{d}_{\text{out}}^\dagger(t) + e^{-i\varphi} e^{i\tilde{\omega}_{\text{pr}}t} \hat{d}_{\text{out}}(t) \right], \quad (\text{S22})$$

where the angle φ determines the measured quadrature and will be specified later. For the two eigenstates $\hat{\sigma}_z |\sigma_z\rangle = \sigma_z |\sigma_z\rangle$ with $\sigma_z \in \{+1, -1\}$, the optical output field will evolve into two different coherent states. They give rise to different integrated homodyne currents $\langle \hat{\mathcal{I}}(\tau) \rangle_\varepsilon$, where $\langle \cdot \rangle_\varepsilon$ denotes an expectation value with the mechanical resonance frequency being shifted by $\varepsilon = -\chi\sigma_z$. Since the instantaneous homodyne current fluctuates about its expectation value, this signal will be accompanied by state-dependent noise $\langle [\delta\hat{\mathcal{I}}(\tau)]^2 \rangle_\varepsilon$, where $\delta\hat{\mathcal{I}}(\tau) = \hat{\mathcal{I}}(\tau) - \langle \hat{\mathcal{I}}(\tau) \rangle_\varepsilon$. The signal-to-noise ratio (SNR) of the spin readout process is then given by

$$\text{SNR}^2(\tau) = \frac{\text{S}^2(\tau)}{\text{N}^2(\tau)} = \frac{\left| \langle \hat{\mathcal{I}}(\tau) \rangle_{-\chi} - \langle \hat{\mathcal{I}}(\tau) \rangle_{+\chi} \right|^2}{\langle [\delta\hat{\mathcal{I}}(\tau)]^2 \rangle_{-\chi} + \langle [\delta\hat{\mathcal{I}}(\tau)]^2 \rangle_{+\chi}}, \quad (\text{S23})$$

which can be evaluated using Eqs. (S21) and (S22). The exact expressions for the signal-to-noise ratio are quite lengthy but they can be simplified by the following observation. After switching on the weak probe laser (S14), the field in the optical cavity will build up on a timescale $1/\kappa \ll 1/\Gamma_{\text{mech}}$. During this time, the mechanical mode is still

at rest and the optical output signal carries no information on the mechanical frequency shift ε . Information on ε will only start to be present in the optical output signal when the mechanical motion rings up. We can get rid of the short-time dynamics of the cavity field by taking the usual limit $\kappa \gg G, \chi, \Gamma_{\text{mech}}$ while keeping the optomechanical cooperativity C_{om} fixed. This simplifies the expressions significantly and we find

$$\left| \langle \hat{\mathcal{I}}(\tau) \rangle_{-\chi} - \langle \hat{\mathcal{I}}(\tau) \rangle_{+\chi} \right|^2 = \frac{8\sqrt{\kappa} |a_{\text{pr,in}}| \Gamma_{\text{mech}} C_{\text{om}}}{|z_-|^2 |z_+|^2} \left| z_-^2 - (z_+^*)^2 - 2i\chi\tau z_- z_+^* + (z_+^*)^2 e^{-z_- \tau/2} - z_-^2 e^{-(z_+^*)\tau/2} \right| \times \cos[\zeta(\tau) - \varphi + \arg(a_{\text{pr,in}})] , \quad (\text{S24})$$

$$\langle [\delta \hat{\mathcal{I}}(\tau)]^2 \rangle_{\pm\chi} = \kappa \left[\tau - \frac{4\Gamma_{\text{mech}} C_{\text{om}} n_{\text{th}}}{1 + C_{\text{om}}} \frac{(z_+^*)^2 (2 - 2e^{-z_+ \tau/2} - z_+ \tau) + z_+^2 (2 - 2e^{-z_+^* \tau/2} - z_+^* \tau)}{|z_+|^4} \right] , \quad (\text{S25})$$

$$\zeta(\tau) = \arg \left[\frac{\sqrt{\kappa} \Gamma_{\text{mech}} C_{\text{om}} |a_{\text{pr,in}}|}{(z_-)^2 (z_+^*)^2} \left(z_-^2 - (z_+^*)^2 - 2i\chi\tau z_- z_+^* + (z_+^*)^2 e^{-z_- \tau/2} - z_-^2 e^{-z_+^* \tau/2} \right) \right] , \quad (\text{S26})$$

where we used the abbreviation $z_{\pm} = \Gamma_{\text{mech}}(1 + C_{\text{om}}) + 2i(\chi \pm \delta)$ and defined the detuning $\delta = \omega_{\text{pr}} - \omega_{\text{o}}$ between the probe laser and the optical cavity resonance frequency. Note that the remaining prefactors $\sqrt{\kappa}$ and κ are due to the prefactor in Eq. (S22) and will cancel in the signal-to-noise ratio. The SNR is thus independent of the optical decay rate κ , as expected.

The SNR is maximized if one measures the homodyne quadrature $\varphi(\tau) = \zeta(\tau) - \arg(a_{\text{pr,in}})$ and if the weak probe laser is resonant with the optical cavity, $\delta = 0$. In this case, signal and noise take the following simple expressions.

$$S(\tau) = 4\sqrt{\kappa} |a_{\text{pr,in}}| \frac{C_{\text{om}}}{1 + C_{\text{om}}} \tau \sin(2\xi) [1 - F(\tau)] , \quad (\text{S27})$$

$$F(\tau) = \frac{1}{\chi\tau} \left[\sin(2\xi) - \sin(2\xi + \chi\tau) e^{-\Gamma_{\text{mech}}(1+C_{\text{om}})\tau/2} \right] , \quad (\text{S28})$$

$$N(\tau) = \sqrt{2\kappa\tau [1 - G(\tau)]} , \quad (\text{S29})$$

$$G(\tau) = 8n_{\text{th}}\Gamma_{\text{mech}} \frac{C_{\text{om}}}{1 + C_{\text{om}}} \frac{2\cos(2\xi) - 2\chi\tau \cos(\xi) / \sin(\xi) - 2\cos(2\xi + \chi\tau) e^{-\Gamma_{\text{mech}}(1+C_{\text{om}})\tau/2}}{4\chi^2\tau / \sin^2(\xi)} , \quad (\text{S30})$$

$$\xi = \arctan \left[\frac{2\chi}{\Gamma_{\text{mech}}(1 + C_{\text{om}})} \right] . \quad (\text{S31})$$

Note that Eqs. (S27) and (S28) are very similar to the corresponding results for dispersive qubit readout in cavity QED [see, e.g., [44] for a detailed discussion but note that Eq. (S15) in the supplemental material of [44] contains a typo and the correct prefactor of the square brackets should be $1/\chi\tau$]. The main difference between our results and the ones in circuit QED are:

- The signal (S27) has an additional prefactor $C_{\text{om}}/(1 + C_{\text{om}})$, which captures the fact that we can tune how much information on the mechanical mode is contained in the optical output field by changing the amplitude of the pump laser.
- The fixed decay rate of the microwave cavity has been replaced by the optically tuneable total mechanical damping rate $\Gamma_{\text{mech}}(1 + C_{\text{om}})$.
- The mechanical response filters the white mechanical input noise given by Eqs. (S16) and (S17), such that the noise in the optical output field is no longer white if $n_{\text{th}} \neq 0$, see Eq. (S30).

To find the shortest measurement rate, we need to maximize the SNR with respect to the optomechanical cooperativity C_{om} (i.e., the pump laser amplitude). There will be a nontrivial optimum since the optical output field does not contain any information on ε both for very small and for very large cooperativities: For $C_{\text{om}} \rightarrow 0$ mechanical and optical mode are decoupled whereas, for $C_{\text{om}} \rightarrow \infty$, the mechanical mode is strongly damped and does not oscillate.

Note that, at short times and for $n_{\text{th}} = 0$, the SNR scales $\propto \tau^{5/2}$ because the mechanics needs to ring up before its state-dependent rotation can discriminate between the two spin states. The square brackets in Eq. (S22) thus grow $\propto \tau^2$. This result is integrated once with respect to time and divided by the noise, which is purely diffusive at zero temperature, i.e., $\propto \sqrt{\tau}$.

III. CRITICAL PHONON NUMBER

We now analyze the validity of the approximations made in the derivation of the SNR, given by Eqs. (S27) to (S31). From Eq. (S18), we obtain the mechanical phonon number n_{mech} and the intracavity photon number n_{cav} due to the optical probe laser, which are given by the following expressions for $\delta = 0$ and $\kappa \gg G, \chi, \Gamma_{\text{mech}}$:

$$n_{\text{mech}}(t) = \left| \langle \hat{d}(t) \rangle_\varepsilon \right|^2 = \frac{4\Gamma_{\text{mech}}C_{\text{om}} |a_{\text{pr,in}}|^2}{\Gamma_{\text{mech}}^2(1+C_{\text{om}})^2 + 4\varepsilon^2} \left(1 + e^{-\Gamma_{\text{mech}}(1+C_{\text{om}})t} - 2\cos(\varepsilon t)e^{-\Gamma_{\text{mech}}(1+C_{\text{om}})t/2} \right), \quad (\text{S32})$$

$$n_{\text{cav}}(t) = \left| \langle \hat{b}(t) \rangle_\varepsilon \right|^2 = \frac{4|a_{\text{pr,in}}|^2}{\kappa[\Gamma_{\text{mech}}^2(1+C_{\text{om}})^2 + 4\varepsilon^2]} \left[\Gamma_{\text{mech}}C_{\text{om}}e^{-\Gamma_{\text{mech}}(1+C_{\text{om}})t/2} (2\Gamma_{\text{mech}}\cos(\varepsilon t) - 4\varepsilon\sin(\varepsilon t)) \right. \\ \left. + \Gamma_{\text{mech}}^2 + 4\varepsilon^2 + \Gamma_{\text{mech}}^2C_{\text{om}}^2e^{-\Gamma_{\text{mech}}(1+C_{\text{om}})t} \right]. \quad (\text{S33})$$

Note that their ratio is $n_{\text{mech}}(t)/n_{\text{cav}}(t) \propto \kappa/\Gamma_{\text{mech}} \gg 1$, i.e., even a small intracavity photon number leads to a very large mechanical phonon number. Various assumptions of our derivation in Sec. I may break down if the mechanical phonon number becomes too large:

First, nonlinearities of the of the mechanical mode may become relevant if the root-mean-square (RMS) amplitude of oscillation becomes comparable to the dimensions of the OMC. Given zero-point fluctuations $x_{\text{zpf}} \approx 1 - 10$ fm and devices of the order of micrometers [28, 65], mechanical nonlinearities will only show up at extremely high phonon numbers $n_{\text{mech}} \approx \mathcal{O}(10^{16})$.

Second, already at lower phonon numbers, the linearization of the optomechanical interaction used to derive Eq. (S11) may break down. In a frame where both \hat{d} and \hat{b} oscillate at ω_m , the counter-rotating terms neglected in Eq. (S11) are

$$\hat{H}_{\text{om}}^{\text{cr}} = -G \left(e^{-2i\omega_m t} \hat{d}\hat{b} + e^{2i\omega_m t} \hat{d}^\dagger\hat{b}^\dagger \right) - g_0 \hat{d}^\dagger \hat{d} \left(e^{-i\omega_m t} \hat{b} + e^{i\omega_m t} \hat{b}^\dagger \right). \quad (\text{S34})$$

Their contribution to the dynamics is negligible if the conditions

$$G\sqrt{n_{\text{mech}}} \ll 2\omega_m \quad \text{and} \quad g_0\sqrt{n_{\text{mech}}} \ll \omega_m \quad (\text{S35})$$

hold, which are equivalent to $n_{\text{mech}} \ll 10^6/C_{\text{om}}$ and $n_{\text{mech}} \ll 10^9$, respectively. Both conditions are satisfied for our parameters, as shown by the inset of Fig. 2 in the main text.

Third, we need to ensure that higher-order corrections to the dispersive spin-mechanical coupling remain negligible. This turns out to be the most restrictive constraint on our system. From Eq. (S5), we see that higher-order terms in the Schrieffer-Wolff transformation remain negligible if the condition

$$\frac{g_{\text{sm}}}{\Delta_{\text{sm}}} \sqrt{n_{\text{mech}}} \ll 1, \quad (\text{S36})$$

holds, which can be satisfied by choosing a sufficiently large spin-mechanical detuning Δ_{sm} . A conservative estimate on the maximum drive amplitude $|a_{\text{pr,in}}|$ can be obtained by considering the steady-state value of Eq. (S32),

$$n_{\text{mech}}^{\text{ss}} \equiv \lim_{\tau \rightarrow \infty} n_{\text{mech}}(\tau) = \frac{4\Gamma_{\text{mech}}C_{\text{om}} |a_{\text{pr,in}}|^2}{\Gamma_{\text{mech}}^2(1+C_{\text{om}})^2 + 4\varepsilon^2}. \quad (\text{S37})$$

For $\chi \ll \Gamma_{\text{mech}}$, this equation will determine the mechanical phonon number at τ_{meas} whereas, for $\chi \gtrsim \Gamma_{\text{mech}}$, a SNR of unity may be obtained even before the phonon number approaches this steady-state value. Using $\varepsilon^2 = \chi^2$, we thus find

$$|a_{\text{pr,in}}^{\text{cr}}|^2 \geq \left(\frac{\Delta_{\text{sm}}}{g_{\text{sm}}} \right)^2 \frac{\Gamma_{\text{mech}}^2(1+C_{\text{om}})^2 + 4\chi^2}{4\Gamma_{\text{mech}}C_{\text{om}}} \geq \left(\frac{\Delta_{\text{sm}}}{g_{\text{sm}}} \right)^2 \frac{\Gamma_{\text{mech}}}{2} \left(\sqrt{1 + \frac{4\chi^2}{\Gamma_{\text{mech}}^2}} + 1 \right), \quad (\text{S38})$$

where we minimized the expression over C_{om} in the last step. We choose our system parameters such that $n_{\text{mech}} < n_{\text{mech}}^{\text{crit}}$ for all considered plot values, see the inset of Fig. 2 of the main text. In particular, for the SiV parameters given in the main text, this amounts to $|a_{\text{pr,in}}^{\text{cr}}|^2/\sqrt{\Gamma} \geq 30$ and $n_{\text{mech}}^{\text{crit}} \approx 5700$, compared to an actual phonon number of $n_{\text{mech}}(\tau_{\text{meas}}) = 137$.

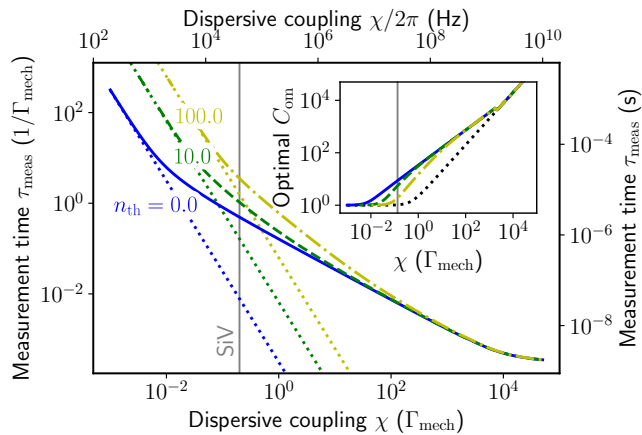


FIG. S1. Minimum measurement time required to reach a SNR of unity in the presence of a finite-temperature mechanical bath. The solid blue curve is the same as in Fig. 2 of the main text, $a_{\text{pr,in}}/\sqrt{\Gamma_{\text{mech}}} = 20.0$ and $n_{\text{th}} = 0$. The green (yellow) curve are for increasing thermal phonon number but fixed $a_{\text{pr,in}}/\sqrt{\Gamma_{\text{mech}}} = 20.0$. The inset shows the optimal cooperativity C_{om} minimizing τ_{meas} . As C_{om} grows, optomechanical cooling compensates the nonzero thermal phonon number n_{th} , and the zero-temperature limit is recovered for $\chi/\Gamma_{\text{mech}} \gg 1$.

IV. FINITE-TEMPERATURE CASE

The case of a zero-temperature environment assumed in the main text is an excellent approximation for the optical mode. However, the mechanical mode of the OMC may have a nonzero thermal occupation n_{th} if the temperature of the environment is not small compared to ω_{m} or if the OMC is heated due to optical absorption. The SNR has then the form

$$\text{SNR}^2(\tau, n_{\text{th}}) = \frac{\text{SNR}^2(\tau, 0)}{1 - G(\tau)}, \quad (\text{S39})$$

where $\text{SNR}^2(\tau, 0)$ is the zero-temperature SNR given in Eq. (4) of the main text and $G(\tau)$ is defined in Eq. (S30). The function $G(\tau)$ captures the fluctuations at finite temperature and has the limits

$$\lim_{n_{\text{th}} \rightarrow 0} G(\tau) = 0, \quad (\text{S40})$$

$$\lim_{\tau \rightarrow \infty} G(\tau) = -2n_{\text{th}}, \quad (\text{S41})$$

$$\lim_{\chi \rightarrow \infty} G(\tau) = 0. \quad (\text{S42})$$

If the integration time is much longer than the mechanical ringup time, $\tau_{\text{meas}} \gg 1/\Gamma_{\text{mech}}$, $G(\tau)$ has decayed to its steady-state value such that the noise is purely diffusive and simply enhanced by a factor $\sqrt{1 + 2n_{\text{th}}}$, i.e., $N(\tau) = \sqrt{2\kappa\tau(1 + 2n_{\text{th}})}$. Thus, for $\chi \ll \Gamma_{\text{mech}}$, the impedance-matching condition $C_{\text{om}} = 1$ will be unchanged and the measurement time is

$$\tau_{\text{meas}} \rightarrow \frac{\Gamma_{\text{mech}}^2}{8|a_{\text{pr,in}}|^2 \chi^2} (1 + 2n_{\text{th}}), \quad (\text{S43})$$

which generalizes Eq. (5) of the main text. For $\chi \gtrsim \Gamma_{\text{mech}}$, the transient dynamics becomes relevant and $G(\tau)$ depends explicitly on the integration time. However, the optimal cooperativity in this regime increases, $C_{\text{om}} > 1$, which leads to an increased optomechanical cooling and effectively reduces n_{th} . For $C_{\text{om}} \gg 1$, $\chi/\Gamma_{\text{mech}}$, one can show that

$$G(\tau) \approx 8 \frac{n_{\text{th}}}{C_{\text{om}}} \frac{2 - x - 2e^{-x/2}}{x}, \quad (\text{S44})$$

where $x = \Gamma_{\text{mech}} C_{\text{om}} \tau$. Since $[2 - x - 2e^{-x/2}]/x \in [-1, 0]$, optomechanical cooling will dominate if $C_{\text{om}} \gtrsim 10n_{\text{th}}$, such that we recover the zero-temperature result $G(\tau) \rightarrow 0$. In particular, the fundamental limit deep in the strong-dispersive-coupling regime, $\chi/\Gamma_{\text{mech}} \gg 1, n_{\text{th}}$,

$$\tau_{\text{meas}} \rightarrow \frac{1}{8|a_{\text{pr,in}}|^2}, \quad (\text{S45})$$

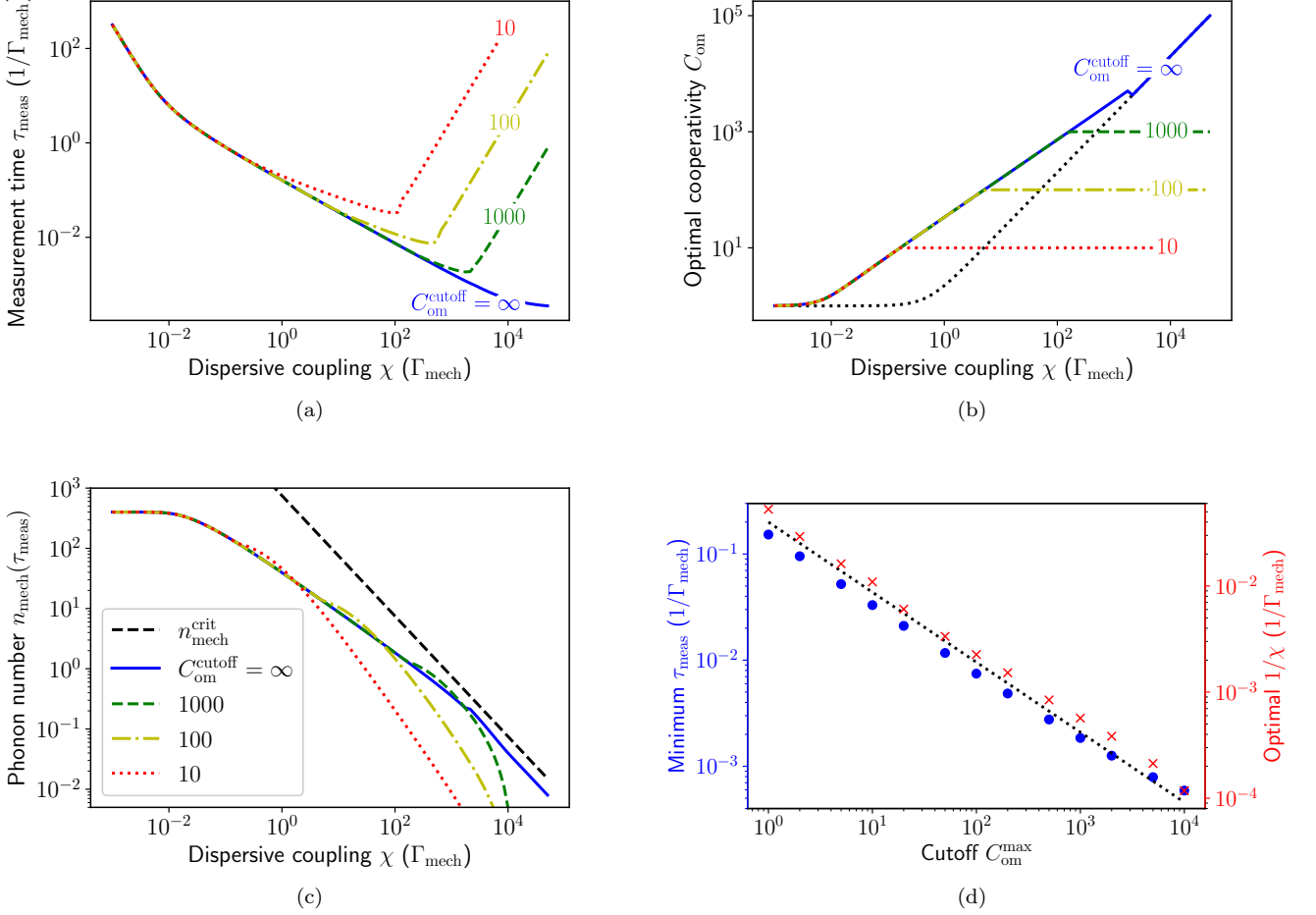


FIG. S2. Single-spin readout with a constrained optomechanical cooperativity. (a) Minimum measurement time τ_{meas} as a function of the dispersive coupling strength. The blue curve shows the data of Fig. 2 of the main text for $a_{\text{pr,in}}/\sqrt{\Gamma_{\text{mech}}} = 20.0$ and $n_{\text{th}} = 0$. For all curves, the cooperativity C_{om} has been optimized with a constraint $C_{\text{om}} \leq C_{\text{om}}^{\text{cutoff}}$ indicated by the labels. (b) Corresponding optimal cooperativity. The dotted black line indicates the optimal cooperativity $C_{\text{om}} = \sqrt{1 + 4\chi^2/\Gamma_{\text{mech}}^2}$ if transient dynamics can be ignored. (c) Corresponding mechanical phonon number $n_{\text{mech}}(\tau_{\text{meas}})$ as a function of χ . Like in the inset of Fig. 2 of the main text, the black dashed curve indicating the critical phonon number has been calculated by varying g_{sm} while keeping the spin-mechanical detuning $\Delta_{\text{sm}}/\Gamma_{\text{mech}} = 750$ fixed, and using $\kappa/\Gamma_{\text{mech}} = 10000$. (d) Global minimum of the measurement times as a function of χ shown in (a) (blue dots, left axis) and the corresponding values of χ (red crosses, right axis). The dotted black line indicates a $1/C_{\text{om}}^{2/3}$ scaling with prefactor 0.2 (left axis) and 0.04 (right axis).

is the same as for the zero-temperature case, see Eq. (6) of the main text. This crossover to a zero-temperature result is illustrated in Fig. S1, where we plot the minimum measurement time and the corresponding optimal cooperativity for different thermal phonon numbers n_{th} . Interestingly, the range of χ values for which $C_{\text{om}} \approx 1$ grows with n_{th} . This means that, for small $\chi \ll \Gamma$, it is more beneficial to maintain the impedance-matching condition $C_{\text{om}} = 1$ (which maximizes the output signal) than to increase C_{om} (which would enhance the optomechanical cooling at the expense of a reduced signal).

V. BOUNDED OPTOMECHANICAL COOPERATIVITY

The discussion in the main text suggest that the optimal cooperativity diverges with increasing dispersive coupling, $C_{\text{om}} \rightarrow 2\chi/\Gamma_{\text{mech}}$. However, such a scaling is not realistic for the following two reasons. First, from an experimental point of view, the optical cooperativity will be bounded from above by the available laser power as well as the maximum heating rate tolerable by the optomechanical crystal and the optical components in the setup. Second, from a theoretical point of view, correction terms to the derivation in Sec. I will become relevant if the optically-

enhanced coupling strength G approaches the strong-coupling regime $G \gtrsim \kappa$ [66]. For the chosen parameters, this will occur if $C_{\text{om}} \gtrsim 4 \times 10^4$. Therefore, we also provide simulations of τ_{meas} , C_{om} , and $n_{\text{mech}}(\tau_{\text{meas}})$ with different cutoffs on C_{om} , which are shown in Fig. S2.

As soon as the cooperativity reaches the cutoff value, the decrease of τ_{meas} with increasing $\chi/\Gamma_{\text{mech}}$ slows down, followed by a sharp increase of τ_{meas} for even larger values of the dispersive coupling [see Fig. S2(a)]. At the same time, $n_{\text{mech}}(\tau_{\text{meas}})$ decreases below its value in the case of no cutoff [see Fig. S2(c)]. These effects can be understood by the following intuitive picture. In the transient regime, C_{om} is increased beyond unity to increase the mechanical damping rate and thus to speed up the mechanical response to the weak probe laser. A bound on the cooperativity prevents reaching the optimal value of the enhanced mechanical damping rate but still leads to a reduction of the overall measurement time τ_{meas} compared to the case with $C_{\text{om}} = 1$. At the same time, the increased mechanical damping rate ensures that the mechanical mode (whose resonance frequency is shifted to $\omega_m \pm \chi$ depending on the spin state) can still be driven by the optical probe laser at frequency ω_m . If the dispersive coupling is increased significantly beyond $\chi \approx \Gamma_{\text{mech}} C_{\text{om}}^{\text{cutoff}}$, the mechanical mode is too off-resonant to be driven by the probe laser, n_{mech} drops, and the measurement time increases strongly.

In Fig. S2(d), we show the minimum achievable measurement times at the kink of the curves in Fig. S2(a), and the corresponding optimal values of the dispersive coupling strength.

VI. ESTIMATED STRAIN COUPLING FOR SiV DEFECTS

In this section, we estimate the strain coupling of an SiV defect in the presence of a magnetic field. The negatively charged SiV center is an interstitial point defect in the diamond lattice where two carbon atoms have been replaced by a silicon atom. We chose the axis between the missing carbon atoms to be the z axis. The silicon atom is placed along the z axis in the middle between the two missing carbon atoms, such that the entire defect has an inversion symmetry about the position of the silicon atom. Therefore, the SiV defect belongs to the D_{3d} point group, and its electronic orbitals have A or E symmetry and can have even (g) or odd (u) parity with respect to inversion about the Si position [67, 68]. In the ground (excited) state, an unpaired hole is in the e_{gx}, e_{gy} (e_{ux}, e_{uy}) orbitals, each of which is twofold degenerate due to the spin degree of freedom. The resulting four-fold degeneracy of the ground-state and excited-state manifolds is partially lifted by the spin-orbit (SO) interaction, which splits the ground-state (excited-state) manifold into two spin-degenerate doublets separated by a spin-orbit splitting $\lambda_{\text{SO},g} \approx 46$ GHz ($\lambda_{\text{SO},u} \approx 255$ GHz). For each manifold $\alpha \in \{g, u\}$, the spin-orbit Hamiltonian is

$$\hat{H}_{\text{SO},\alpha} = -\frac{\lambda_{\text{SO},\alpha}}{2} \hat{L}_z^{(\alpha)} \otimes \hat{S}_z, \quad (\text{S46})$$

where the z component of the orbital angular momentum operator in the basis $\{|e_{\alpha x}\rangle, |e_{\alpha y}\rangle\}$ is [69]

$$\hat{L}_z^{(\alpha)} = \begin{pmatrix} 0 & -i \\ i & 0 \end{pmatrix}, \quad (\text{S47})$$

and the z component of the spin operator is $\hat{S}_z = |\uparrow\rangle\langle\uparrow| - |\downarrow\rangle\langle\downarrow|$. In the absence of strain or magnetic fields, $\hat{H}_{\text{SO},\alpha}$ is diagonal in the basis $\{|e_{\alpha-}\downarrow\rangle, |e_{\alpha+}\uparrow\rangle, |e_{\alpha+}\downarrow\rangle, |e_{\alpha-}\uparrow\rangle\}$ with eigenvalues $\{-\lambda_{\text{SO},\alpha}/2, -\lambda_{\text{SO},\alpha}/2, +\lambda_{\text{SO},\alpha}/2, +\lambda_{\text{SO},\alpha}/2\}$. The orbital eigenstates are defined as $|e_{\alpha\pm}\rangle = \mp(|e_{\alpha x}\rangle \pm i|e_{\alpha y}\rangle)/\sqrt{2}$, where the subscripts \pm denote the orbital-angular-momentum projection of the states, $\hat{L}_z^{(\alpha)} |e_{\alpha\pm}\rangle = \pm |e_{\alpha\pm}\rangle$.

The remaining degeneracies are lifted by magnetic fields and strain, which are modeled by the following Hamiltonians [18, 69],

$$\hat{H}_{Z,\alpha} = \gamma_L B_z \hat{L}_z^{(\alpha)} \otimes \hat{\mathbf{1}} + \gamma_S \hat{\mathbf{1}}^{(\alpha)} \otimes (B_x \hat{S}_x + B_y \hat{S}_y + B_z \hat{S}_z), \quad (\text{S48})$$

$$\hat{H}_{\text{strain},\alpha} = \left[\varepsilon_{A_{1g}}^\alpha (|e_{\alpha x}\rangle\langle e_{\alpha x}| + |e_{\alpha y}\rangle\langle e_{\alpha y}|) + \varepsilon_{E_{gx}}^\alpha (|e_{\alpha x}\rangle\langle e_{\alpha x}| - |e_{\alpha y}\rangle\langle e_{\alpha y}|) + \varepsilon_{E_{gy}}^\alpha (|e_{\alpha x}\rangle\langle e_{\alpha y}| + |e_{\alpha y}\rangle\langle e_{\alpha x}|) \right] \otimes \hat{\mathbf{1}}, \quad (\text{S49})$$

where $\hat{S}_x = |\uparrow\rangle\langle\downarrow| + |\downarrow\rangle\langle\uparrow|$ and $\hat{S}_y = (|\uparrow\rangle\langle\downarrow| - |\downarrow\rangle\langle\uparrow|)/i$. The energies $\varepsilon_{A_{1g}}^\alpha$, $\varepsilon_{E_{gx}}^\alpha$, and $\varepsilon_{E_{gy}}^\alpha$ depend on the strain tensor decomposed in terms of the irreducible representations of the D_{3d} point group, and the associated strain susceptibilities of the $\alpha \in \{g, u\}$ manifolds,

$$\varepsilon_{A_{1g}}^\alpha = t_\perp^\alpha (\epsilon_{xx} + \epsilon_{yy}) + t_\parallel^\alpha \epsilon_{zz}, \quad (\text{S50})$$

$$\varepsilon_{E_{gx}}^\alpha = d^\alpha (\epsilon_{xx} - \epsilon_{yy}) + f^\alpha \epsilon_{zx}, \quad (\text{S51})$$

$$\varepsilon_{E_{gy}}^\alpha = -2d^\alpha \epsilon_{xy} + f^\alpha \epsilon_{yz}, \quad (\text{S52})$$

where the strain susceptibilities are $d^g = 1.3$ PHz/strain as well as $f^g = -1.7$ PHz/strain, and the gyromagnetic ratios are $\gamma_L = 0.1 \times 14$ GHz/T and $\gamma_S = 14$ GHz/T [18]. The difference of the strain susceptibilities t_{\parallel}^{α} and t_{\perp}^{α} for the g and e manifolds have been measured in Ref. 18, too, but they are not important here since the $\varepsilon_{A_{1g}}^{\alpha}$ terms will be irrelevant in the following analysis.

The total Hamiltonian in the α manifold, expressed in the SO eigenbasis $\{|e_{\alpha-} \downarrow\rangle, |e_{\alpha+} \uparrow\rangle, |e_{\alpha+} \downarrow\rangle, |e_{\alpha-} \uparrow\rangle\}$ is thus

$$\hat{H}_{\alpha} = \begin{pmatrix} -\frac{\lambda_{\text{SO},\alpha}}{2} - (\gamma_S + \gamma_L)B_z & 0 & -\varepsilon_{E_{gx}}^{\alpha} - i\varepsilon_{E_{gy}}^{\alpha} & \gamma_S(B_x + iB_y) \\ 0 & -\frac{\lambda_{\text{SO},\alpha}}{2} + (\gamma_S + \gamma_L)B_z & \gamma_S(B_x - iB_y) & -\varepsilon_{E_{gx}}^{\alpha} + i\varepsilon_{E_{gy}}^{\alpha} \\ -\varepsilon_{E_{gx}}^{\alpha} + i\varepsilon_{E_{gy}}^{\alpha} & \gamma_S(B_x + iB_y) & +\frac{\lambda_{\text{SO},\alpha}}{2} - (\gamma_S - \gamma_L)B_z & 0 \\ \gamma_S(B_x - iB_y) & -\varepsilon_{E_{gx}}^{\alpha} - i\varepsilon_{E_{gy}}^{\alpha} & 0 & +\frac{\lambda_{\text{SO},\alpha}}{2} + (\gamma_S - \gamma_L)B_z \end{pmatrix} + \varepsilon_{A_{1g}}^{\alpha} \hat{\mathbb{1}}_{4 \times 4}. \quad (\text{S53})$$

Our goal is to identify an effective two-level system within the ground-state manifold of \hat{H}_{α} . We therefore set $\alpha = g$ in the following and suppress this subscript for simplicity. We also ignore the $\varepsilon_{A_{1g}}^{\alpha}$ term, which only contributes a constant energy shift of the g and u manifolds, and we set $B_y = 0$. Both the Zeeman and the strain terms mix different SO eigenstates. However, for SiV defects in a diamond OMC, the Zeeman terms will be of the order of GHz (i.e., comparable to the SO splitting) whereas the strain terms will be of the order of MHz. We therefore diagonalize $\hat{H}_{\text{SO}} + \hat{H}_{\text{Z}}$ and treat the strain terms \hat{H}_{strain} perturbatively. The eigenvectors of $\hat{H}_{\text{SO}} + \hat{H}_{\text{Z}}$ will be denoted by $|e_{\tau}\sigma\rangle'$ with $\tau \in \{+, -\}$ and $\sigma \in \{\uparrow, \downarrow\}$, where $|e_{\tau}\sigma\rangle$ is the corresponding eigenstate of \hat{H}_{SO} to which $|e_{\tau}\sigma\rangle'$ reduces in the limit of vanishing magnetic field. The associated energies are

$$E_{\tau,\sigma} = \tau \left[\gamma_L B_z - \frac{2\delta_{\sigma,\uparrow} - 1}{2} \sqrt{4\gamma_S^2 B_x^2 + (\lambda_{\text{SO}} - 2\tau\gamma_S B_z)^2} \right], \quad (\text{S54})$$

where $\delta_{\sigma,\sigma'}$ denotes the Kronecker delta. A purely off-axis magnetic field, $B_z = 0$ but $B_x \neq 0$, simply shifts the $|e_{-} \downarrow\rangle'$ and $|e_{+} \uparrow\rangle'$ levels with respect to the $|e_{+} \downarrow\rangle'$ and $|e_{-} \uparrow\rangle'$ levels, but does not lift their respective degeneracy. We thus need a finite B_z component, too, to define an effective two-level system using the $|e_{-} \downarrow\rangle'$ and $|e_{+} \uparrow\rangle'$ levels. This two-level system should maintain a fixed detuning from the mechanical mode of the OMC, i.e., $E_{+, \uparrow} - E_{-, \downarrow} = \omega_s = \omega_m - \Delta_{\text{sm}}$ should be independent of the chosen magnetic field. For $\omega_s / [2(\gamma_L + \gamma_S)] \leq B_z \leq \omega_s / (2\gamma_L)$, this condition can be satisfied by choosing the B_x component as

$$|B_x| = \frac{\sqrt{(2\gamma_S B_z)^2 - (2\gamma_L B_z - \omega_s)^2} \sqrt{\lambda_{\text{SO}}^2 - (2\gamma_L B_z - \omega_s)^2}}{2\gamma_S |2\gamma_L B_z - \omega_s|}. \quad (\text{S55})$$

For $B_z \gtrsim \omega_s / [(2\gamma_L + \gamma_S)]$, $\gamma_S \gg \gamma_L$, and $\lambda_{\text{SO}} \gg \omega_s$, the off-axis magnetic field scales approximately as

$$|B_x| \approx \frac{\lambda_{\text{SO}}}{\sqrt{\gamma_S \omega_s}} \sqrt{B_z - \frac{\omega_s}{2\gamma_S}}. \quad (\text{S56})$$

The B_x field increases very quickly with growing B_z , which can be understood by the following intuitive argument. For simplicity, we consider the limit $\gamma_L \rightarrow 0$, i.e., the Zeeman splitting of the high-energy ($|e_{\alpha+} \downarrow\rangle$ and $|e_{\alpha-} \uparrow\rangle$, at energy $\lambda_{\text{SO}}/2$) and low-energy ($|e_{\alpha-} \downarrow\rangle$ and $|e_{\alpha+} \uparrow\rangle$, at energy $-\lambda_{\text{SO}}/2$) spin-orbit doublet is identical. The minimum B_z field which yields a real solution for B_x is $B_z = \omega_s / 2\gamma_S$, i.e., the magnetic field parallel to the SiV axis splits the doublets just enough to generate the desired level splitting ω_s . For a 7 GHz transition frequency, this happens at $B_z = 0.5$ T. If the B_z field is further increased, the transition frequency $E_{+, \uparrow} - E_{-, \downarrow}$ is larger than ω_s and one needs an off-axis magnetic field B_x to compensate the mismatch. This is possible because the B_x field causes separate avoided level crossings between the the outer ($|e_{\alpha-} \uparrow\rangle$ and $|e_{\alpha-} \downarrow\rangle$) and inner ($|e_{\alpha+} \downarrow\rangle$ and $|e_{\alpha+} \uparrow\rangle$) Zeeman-split states. For $\gamma_S B_x \gg \lambda_{\text{SO}}$, the upper and lower Zeeman-split states will converge to the energies $\gamma_S B_x$ and $-\gamma_S B_x$, respectively. Therefore, the transition frequencies between the two high-energy states (and, likewise, between the two low-energy states) must ultimately vanish, and the excess detuning caused by the B_z field will be canceled for some intermediate B_x field. The convergence of the transition frequencies will occur if $\gamma_S B_x \gtrsim \lambda_{\text{SO}}$, which yields $B_x \gtrsim 3.3$ T $\gg B_z$.

We now investigate how the perturbation given by the strain Hamiltonian \hat{H}_{strain} affects the eigenstates $\{|e_{\alpha-} \downarrow\rangle', |e_{\alpha+} \uparrow\rangle', |e_{\alpha+} \downarrow\rangle', |e_{\alpha-} \uparrow\rangle'\}$ of $\hat{H}_{\text{SO}} + \hat{H}_{\text{Z}}$. The magnetic field components perpendicular to the z axis mix SO eigenstates with the same orbital projection τ , i.e., $|e_{-} \downarrow\rangle' = c_{-\downarrow\downarrow} |e_{-} \downarrow\rangle + c_{-\downarrow\uparrow} |e_{-} \uparrow\rangle$, $|e_{+} \uparrow\rangle' = c_{+\uparrow\uparrow} |e_{+} \uparrow\rangle + c_{+\uparrow\downarrow} |e_{+} \downarrow\rangle$, etc. In contrast, the strain Hamiltonian mixes SO eigenstates with the same spin projection σ . Therefore,

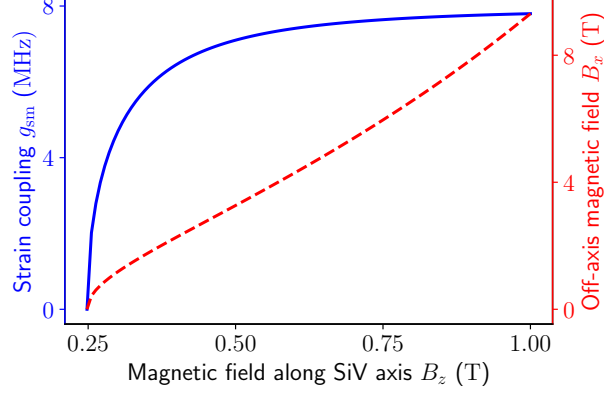


FIG. S3. Strain coupling g_{sm} of the effective two-level system formed by the states $|e_- \downarrow\rangle'$ and $|e_+ \uparrow\rangle'$ as a function of the magnetic field B_z parallel to the SiV axis (solid blue curve). The level splitting of the two-level system is kept constant, $E_{+\uparrow} - E_{-\downarrow} = \omega_s$, by tuning the off-axis magnetic field B_x (dashed red curve), see Eq. (S55). Parameters are $\omega_s = 7.64$ GHz, $\lambda_{\text{SO}} = 46$ GHz, $\gamma_L = 1.4$ GHz/T, $\gamma_S = 14$ GHz/T, $\varepsilon_{E_{gx}} = -7.92$ MHz, and $\varepsilon_{E_{gy}} = 0.0$ MHz.

the strain Hamiltonian rewritten in the basis $\{|e_{\alpha-} \downarrow\rangle', |e_{\alpha+} \uparrow\rangle', |e_{\alpha+} \downarrow\rangle', |e_{\alpha-} \uparrow\rangle'\}$ has the form

$$\hat{H}'_{\text{strain}} = \begin{pmatrix} 0 & c_1(\varepsilon_{E_{gx}} + i\varepsilon_{E_{gy}}) & c_2(\varepsilon_{E_{gx}} + i\varepsilon_{E_{gy}}) & 0 \\ c_1^*(\varepsilon_{E_{gx}} - i\varepsilon_{E_{gy}}) & 0 & 0 & c_3(\varepsilon_{E_{gx}} - i\varepsilon_{E_{gy}}) \\ c_2^*(\varepsilon_{E_{gx}} - i\varepsilon_{E_{gy}}) & 0 & 0 & c_4(\varepsilon_{E_{gx}} - i\varepsilon_{E_{gy}}) \\ 0 & c_3^*(\varepsilon_{E_{gx}} + i\varepsilon_{E_{gy}}) & c_4^*(\varepsilon_{E_{gx}} + i\varepsilon_{E_{gy}}) & 0 \end{pmatrix}, \quad (\text{S57})$$

where the parameters c_1 to c_4 depend on the expansion coefficients $c_{\tau\sigma\sigma'}$. The terms proportional to c_1 couple the two levels $|e_- \downarrow\rangle'$ and $|e_+ \uparrow\rangle'$ of the effective two-level system to the mechanical mode, and they represent the desired strain coupling term. However, the c_2 and c_3 terms also introduce undesired couplings to the other states $|e_+ \downarrow\rangle'$ and $|e_- \uparrow\rangle'$. The energy gap between the upper two-level-system state $|e_+ \uparrow\rangle'$ and the lower state $|e_+ \downarrow\rangle'$ of the remaining states grows with B_z and is at least $\lambda_{\text{SO}} - \gamma_S \omega_s / (\gamma_L + \gamma_S) \approx \lambda_{\text{SO}} \gg \omega_s$. These transitions are thus highly off-resonant and can be ignored in a rotating wave approximation. We therefore obtain a block-diagonal structure of \hat{H}'_{strain} with a well-defined two-level system formed by $\{|e_- \downarrow\rangle', |e_+ \uparrow\rangle'\}$, which is coupled to a mechanical mode with a magnetic-field-tunable coupling strength.

To estimate the strain coupling, we performed COMSOL simulations of a representative diamond OMC structure with the displacement chosen such that the total strain energy was equal to half the zero-point energy of the mechanical mode. The SiV defect was chosen to be centered vertically and laterally, and to be positioned half-way between the central hole and the adjacent hole along the long axis of the OMC. We considered two different SiV orientations in the diamond lattice and found the strain tensor to be of the order of 10^{-9} , giving rise to $\varepsilon_{E_{gx}} = -7.92$ MHz, and $\varepsilon_{E_{gy}} = 0.0$ MHz. The field-dependent strain coupling strength is then given by $g_{\text{sm}} = |c_1(\varepsilon_{E_{gx}} + i\varepsilon_{E_{gy}})| = \mathcal{O}(\text{MHz})$ and is shown in Fig. S3.

Given the large values of g_{sm} , one may worry that the strain coupling deteriorates the coherence properties of the SiV. Generally, above temperatures of about 1 K, the SiV coherence is deteriorated by 50 GHz phonons which can excite the SiV defect to orbital excited states [18]. Operating the setup at temperatures below 100 mK will eliminate this dominant dephasing mechanism and will also suppress thermal occupation of the mechanical mode, since $n_{\text{th}} \ll 1$ for a several GHz mechanical mode. However, a remaining potential source of dissipation is strain-coupling of the two-level system of interest (with $\omega_s \approx$ several GHz) to other mechanical modes of the OMC. A one-dimensional OMC [as sketched in Fig. 1(b) of the main text] has only a pseudo-bandgap (which suppresses only localized modes with mirror symmetry perpendicular to the long axis of the OMC), such that resonant interactions with nonsymmetric and propagating phonon modes may lead to additional relaxation of the SiV center. However, these modes have a lower Q factor, which reduces the spin cooperativity and leads to a suppression of undesired additional decay mechanisms. Finally, dispersive interactions with off-resonant mechanical modes could cause additional dephasing of the SiV center due to thermal phonon-number fluctuations. Even though dephasing is irrelevant for QND readout, it may limit the operation of the SiV as a quantum sensor. However, the associated dephasing rates will be highly suppressed because $n_{\text{th}} \ll 1$.

VII. QUANTUM SENSING USING OMIT

A. Estimation error

In this section, we take a step back and consider our proposed OMIT readout scheme in the broader context of quantum sensing. More specifically, we assume that a signal to be measured couples to the mechanical mode and causes a small shift $\varepsilon \ll \omega_m, \Gamma_{\text{mech}}, \kappa$ of the mechanical resonance frequency. The estimation error for such an infinitesimal signal is given by the fluctuations $\langle [\widehat{\delta\mathcal{I}}]^2 \rangle_\varepsilon$ of the homodyne current, referred back to the signal ε by normalizing with the rate of change $\partial_\varepsilon \langle \hat{\mathcal{I}} \rangle_\varepsilon$ with respect to variations in ε ,

$$(\Delta\varepsilon)^2(\tau) = \lim_{\varepsilon \rightarrow 0} \frac{\langle [\widehat{\delta\mathcal{I}}(\tau)]^2 \rangle_\varepsilon}{|\partial_\varepsilon \langle \hat{\mathcal{I}}(\tau) \rangle_\varepsilon|^2}. \quad (\text{S58})$$

This estimation error is closely related to the SNR introduced in Eq. (3) of the main text,

$$(\Delta\varepsilon)^2(\tau) = \lim_{\varepsilon \rightarrow 0} \frac{\frac{1}{2} \left(\langle [\widehat{\delta\mathcal{I}}]^2 \rangle_{+\varepsilon} + \langle [\widehat{\delta\mathcal{I}}]^2 \rangle_{-\varepsilon} \right)}{\left| \frac{1}{2\varepsilon} \left(\langle \hat{\mathcal{I}} \rangle_{+\varepsilon} - \langle \hat{\mathcal{I}} \rangle_{-\varepsilon} \right) \right|^2} = \lim_{\varepsilon \rightarrow 0} \frac{2\varepsilon^2}{\text{SNR}^2(\tau)}. \quad (\text{S59})$$

Since we are considering the limit of an infinitesimal signal $\varepsilon \rightarrow 0$, the integration time will be much larger than the mechanical ringup time $1/\Gamma_{\text{mech}}$ and we can ignore transient dynamics. The estimation error optimized over the homodyne detection angle φ is

$$(\Delta\varepsilon)^2(\tau) = \frac{[\Gamma^2(1 + C_{\text{om}})^2 + 4\delta^2] [\Gamma^2(1 + C_{\text{om}})^2 + 8n_{\text{th}}\Gamma_{\text{mech}}^2 C_{\text{om}} + 4\delta^2]}{64\Gamma^2 C_{\text{om}}^2 \tau |a_{\text{pr,in}}|^2}, \quad (\text{S60})$$

which can be further optimized by choosing a resonant probe laser, $\delta = 0$, and by choosing the impedance-matching condition $C_{\text{om}} = 1$. We thus find the optimal estimation error

$$(\Delta\varepsilon)_{\text{opt}}^2(\tau) = \frac{\Gamma_{\text{mech}}^2}{4|a_{\text{pr,in}}|^2 \tau} (1 + 2n_{\text{th}}) = \frac{\Gamma_{\text{mech}}}{4n_{\text{mech}}^{\text{ss}} \tau} (1 + 2n_{\text{th}}), \quad (\text{S61})$$

where we used the steady-state phonon number (S37) in the last step.

The OMIT measurement compares the small unknown frequency shift ε to the width of the OMIT dip in the optical output power, which is given by $\Gamma_{\text{mech}}(1 + C_{\text{om}})$: For perfect impedance matching, $C_{\text{om}} = 1$, and no signal, $\varepsilon = 0$, the weak probe laser will resonantly drive the mechanical mode and the semiclassical amplitude of the optical output field will be zero. In the presence of small signal, $\varepsilon \neq 0$, the mechanical mode is slightly detuned from the probe laser and some photons will be emitted into the optical output field, yielding a finite semiclassical amplitude. The phase quadrature of the reflected light is linearly proportional to ε if the condition $\varepsilon \lesssim \Gamma_{\text{mech}}$ holds (which sets the dynamic range of this method). The mechanical decay rate (which is the smallest decay rate in the system) thus sets the “ruler” with which the unknown frequency shift ε is compared. With this picture in mind, the impedance-matching condition marks the optimal tradeoff between having no mechanical-to-optical conversion in the limit $C_{\text{om}} \rightarrow 0$, and an undesired “stretching” of the “ruler”, $\Gamma_{\text{mech}} \rightarrow \Gamma_{\text{mech}}(1 + C_{\text{om}}) \rightarrow \infty$ in the limit $C_{\text{om}} \rightarrow \infty$.

B. Comparison of different detection schemes

It is instructive to compare our OMIT based detection with other methods to detect a small mechanical frequency shift. In all schemes, the mechanical oscillator is driven at frequency ω_m . Its position operator,

$$\hat{x}(t) = \sqrt{2}x_{\text{zpf}} [\hat{x}_{\text{R}}^{\text{mech}}(t) \cos(\omega_m t) + \hat{p}_{\text{R}}^{\text{mech}}(t) \sin(\omega_m t)], \quad (\text{S62})$$

can be decomposed into the mechanical cosine and sine quadratures

$$\hat{x}_{\text{R}}^{\text{mech}}(t) = \frac{1}{\sqrt{2}} (\hat{b}^\dagger e^{-i\omega_m t} + \hat{b} e^{i\omega_m t}), \quad (\text{S63})$$

$$\hat{p}_{\text{R}}^{\text{mech}}(t) = \frac{i}{\sqrt{2}} (\hat{b}^\dagger e^{-i\omega_m t} - \hat{b} e^{i\omega_m t}), \quad (\text{S64})$$

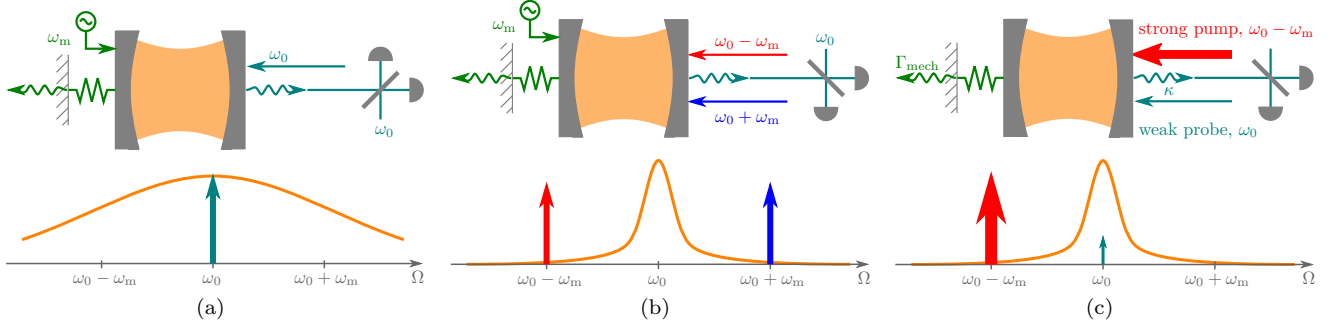


FIG. S4. Comparison of different methods to detect a small mechanical frequency shift $\omega_m \rightarrow \omega_m + \varepsilon$. (a) Optomechanical position measurement, whose estimation error is limited to the standard quantum limit of position detection. (b) Backaction evading (BAE) measurement, which can surpass the standard quantum limit. (c) OMIT readout scheme, which reaches the same estimation error as a BAE measurement with experimentally less demanding requirements.

where x_{zpf} denotes the mechanical zero-point fluctuations. We assume that the phase of the mechanical drive is chosen such that the oscillation of $\langle \hat{x}(t) \rangle$ is purely sinusoidal in the absence of a signal, i.e., $\langle \hat{x}_R^{\text{mech}}(t) \rangle = 0$ for $\varepsilon = 0$. In this case, the cosine quadrature $\hat{x}_R^{\text{mech}}(t)$ is called the *phase quadrature*. A change of the mechanical resonance frequency $\omega_m \rightarrow \omega_m + \varepsilon$ will change the relative phase between the mechanical drive and $\langle \hat{x}(t) \rangle$, such that the phase quadrature $\langle \hat{x}_R^{\text{mech}}(t) \rangle \propto \varepsilon$ becomes nonzero and allows us to infer the frequency shift ε .

a. Direct position measurement Perhaps the most obvious approach to measure $\langle \hat{x}_R^{\text{mech}}(t) \rangle$ is a direct position measurement, which is sketched in Fig. S4(a) and has been analyzed in [51]. The oscillating mechanical position $\hat{x}(t)$ causes a parametric modulation of the optical cavity frequency, $\omega_o(t) = \omega_o[1 - (g_0/\omega_o)\langle \hat{x}(t) \rangle/x_{zpf}]$, which leads to an oscillation of the phase of the light leaving the optical cavity. Depending on the local-oscillator phase, the homodyne detection measures one of the quadratures of the optical output field, which are given by

$$\hat{x}_{R,\text{out}}^{\text{cav}}(t) = \frac{1}{\sqrt{2}}[\hat{d}_{\text{out}}^\dagger(t)e^{-i\omega_o t} + \hat{d}_{\text{out}}(t)e^{+i\omega_o t}] , \quad (\text{S65})$$

$$\hat{p}_{R,\text{out}}^{\text{cav}}(t) = \frac{i}{\sqrt{2}}[\hat{d}_{\text{out}}^\dagger(t)e^{-i\omega_o t} - \hat{d}_{\text{out}}(t)e^{+i\omega_o t}] . \quad (\text{S66})$$

For a suitably chosen phase of the optical input field, the $\hat{p}_{R,\text{out}}^{\text{cav}}$ quadrature of the optical output field is proportional to the mechanical position,

$$\langle \hat{x}_{R,\text{out}}^{\text{cav}}(t) \rangle = 0 , \quad \langle \hat{p}_{R,\text{out}}^{\text{cav}}(t) \rangle = \sqrt{2\Gamma_{\text{mech}}C_{\text{om}}} \frac{\langle \hat{x}(t) \rangle}{x_{zpf}} . \quad (\text{S67})$$

The fundamental limitation of a direct position measurement stems from the fact that it amplifies the non-commuting mechanical quadratures \hat{x}_R^{mech} and \hat{p}_R^{mech} equally by a gain factor $\propto \sqrt{C_{\text{om}}}$. It can thus be understood as a phase-insensitive linear amplifier [70],

$$\hat{d}_{\text{out}}[\omega_m] = -\sqrt{C_{\text{om}}} \frac{2i\Gamma}{\Gamma + 2i\varepsilon} \hat{b}_{\text{in}}[\omega_m] + \text{noise terms} , \quad (\text{S68})$$

where we switched to frequency space by defining the Fourier-transformed operator $\hat{O}[\omega] = \int_{-\infty}^{\infty} dt \hat{O}(t)e^{i\Omega t}$. To ensure that the output modes \hat{d}_{out} and $\hat{d}_{\text{out}}^\dagger$ have proper commutation relations, imprecision noise $n_{\text{add}} \geq 1/2$ has to be added during the amplification step, i.e.,

$$(\Delta\varepsilon)^2(\tau) = \frac{\Gamma_{\text{mech}}}{4n_{\text{mech}}^{\text{ss}}\tau} (2 + 2n_{\text{th}}) . \quad (\text{S69})$$

Assuming thermal noise is negligible, $n_{\text{th}} \rightarrow 0$, the estimation error (S69) for a direct position measurement is thus at least a factor of 2 larger than for our OMIT readout scheme, Eq. (S61). Note that the direct optomechanical position measurement does not require sideband resolution, i.e., it can be implemented in a system having $\kappa \gg \omega_m$. The additional factor of 2 in the estimation error may be a reasonable price to pay for not having to operate in the regime $\kappa \ll \omega_m$.

The fundamental limit $n_{\text{add}} = 1/2$ is called the standard quantum limit of position detection (SQL-PD) [50, 51]. In principle, the SQL-PD also applies to the slope detection technique in atomic-force microscopy (AFM) [41], where one uses a detuned mechanical drive on the slope of the mechanical resonance curve, measures $\langle \hat{x}(t) \rangle$, and infers ε from the amplitude of oscillation. However, current setups are limited by thermal noise, i.e., $n_{\text{th}} \gg 1$. In this limit, Albrecht *et al.* also showed that switching to FM detection, where the mechanical oscillator is driven into limit-cycle motion, does not improve the estimation error over slope detection (but improves the dynamic range) [41]. The same result has been found for sensors using optomechanical limit cycles [49].

b. Backaction-evading measurement The SQL-PD can be surpassed by a backaction-evading (BAE) measurement of $\hat{x}_{\text{R}}^{\text{mech}}(t)$ [52, 53], which is sketched in Fig. S4(b). In this scheme, two laser drives of equal amplitude are applied on the red and blue mechanical sideband. Their relative phase is chosen such that the cavity resonance frequency depends (in a time-average way) only on $\hat{x}_{\text{R}}^{\text{mech}}(t)$, i.e., the interaction term $\propto \hat{a}^\dagger \hat{a} \hat{x}(t)$ is replaced by a term of the form $\hat{a}^\dagger \hat{a} [\hat{x}_{\text{R}}^{\text{mech}}(t) + \text{terms averaging to zero}]$. For a suitably chosen phase of the optical output input field, one now finds

$$\langle \hat{x}_{\text{R,out}}^{\text{cav}}(t) \rangle = 0, \quad \langle \hat{p}_{\text{R,out}}^{\text{cav}}(t) \rangle = \sqrt{\Gamma_{\text{mech}} C_{\text{om}}} \langle \hat{x}_{\text{R}}^{\text{mech}}(t) \rangle. \quad (\text{S70})$$

Unlike direct position detection, only the mechanical $\hat{x}_{\text{R}}^{\text{mech}}(t)$ quadrature is amplified. The BAE scheme thus implements a phase-sensitive amplification scheme, and the equivalent of Eq. (S68) (written in terms of quadrature operators) takes the form,

$$\hat{x}_{\text{R,out}}^{\text{cav}}[0] = 0 + \text{noise terms}, \quad (\text{S71a})$$

$$\hat{p}_{\text{R,out}}^{\text{cav}}[0] = \sqrt{\Gamma_{\text{mech}} C_{\text{om}}} \hat{x}_{\text{R}}^{\text{mech}}[0] + \text{noise terms}. \quad (\text{S71b})$$

Also in the BAE scheme, noise must be added to ensure that the optical output modes have proper canonical commutation relations. However, the amount of added noise is independent of C_{om} and becomes irrelevant in the limit of large gain. The estimation error on changes ε of the mechanical resonance frequency for such a BAE measurement is

$$(\Delta\varepsilon)^2(\tau) = \frac{\Gamma_{\text{mech}}}{4n_{\text{mech}}^{\text{ss}}\tau} \frac{1 + 8C_{\text{om}}(1 + 2n_{\text{th}})}{8C_{\text{om}}} \xrightarrow{C_{\text{om}} \rightarrow \infty} \frac{\Gamma_{\text{mech}}}{4n_{\text{mech}}^{\text{ss}}\tau} (1 + 2n_{\text{th}}). \quad (\text{S72})$$

Hence, in the limit of a large optomechanical cooperativity (i.e., large gain), the optomechanical BAE measurement achieves the same estimation error as our OMIT detection scheme. However, our OMIT detection scheme has an experimentally much more forgiving condition on the required cooperativity, $C_{\text{om}} = 1$. Whereas OMIT-type experiments are routinely used for characterization of optomechanical setups, BAE measurements [54–58] are still much more challenging.

c. OMIT measurement For completeness, we also give the equivalent of Eqs. (S68) and (S71) for the OMIT detection scheme:

$$\hat{d}_{\text{out}}[\omega_{\text{m}}] = \frac{\Gamma_{\text{mech}}(C_{\text{om}} - 1) - 2i\varepsilon}{\Gamma_{\text{mech}}(C_{\text{om}} + 1) + 2i\varepsilon} \hat{d}_{\text{in}}[\omega_{\text{m}}] + \text{noise terms} \quad (\text{S73})$$

Similar to a direct position measurement, OMIT implements a phase-insensitive amplification scheme, but the gain factor never exceeds unity. Therefore, no imprecision noise has to be added to preserve the commutation relations of the output modes and $n_{\text{add}} = 0$ is possible, similar to a BAE measurement in the limit of large gain, $C_{\text{om}} \rightarrow \infty$. Note that the absence of amplification in the OMIT scheme is not a drawback: Unlike optomechanical force sensing, where a small unknown force leads to a tiny change of the mechanical *position* that needs to be amplified for detection, we want to detect a small change of the mechanical resonance frequency, which manifests itself in a change of the *phase* of oscillation. Such a phase change can be probed by driving the mechanical oscillator strongly, which ensures a large output signal and eliminates the need for amplification.

Note that both optomechanical position measurements and BAE detection require a *mechanical* drive whose phase needs to be carefully tuned with respect to the optical local-oscillator used in the homodyne detection setup. In contrast, as shown in Fig. S4(c), our OMIT detection scheme uses the *optical* probe laser as a resonant mechanical drive. Both the weak probe laser and the local-oscillator signal can thus be derived from the same source, which enables a convenient all-optical measurement of the phase of the reflected light. Finally, it is interesting to note that Eq. (S61) is only a factor of $(1 + C_{\text{om}})^2 / C_{\text{om}} = 4$ larger than the estimation error one could obtain in a hypothetical direct mechanical homodyne detection of the phonons dissipated into the substrate (green wiggly arrows in Fig. S4).

C. Impact of imperfect homodyne detection

Experimentally, the estimation error of the OMIT measurement will be limited by the efficiency η of the homodyne detection. Imperfect detection can originate both from the finite efficiency of the photon detectors as well as from scattering and absorption losses on the way to the detector. All these imperfections can be modeled by assuming an additional beamsplitter with transmittivity $\eta < 1$ between the optomechanical system and the detector. The beamsplitter discards a fraction $\sqrt{1-\eta}$ of the optical output field and replaces it with vacuum noise. This increases the estimation error (S61) to

$$(\Delta\varepsilon)^2(\tau) = \frac{\Gamma_{\text{mech}}}{4n_{\text{mech}}^{\text{ss}}\tau} (1 + 2n_{\text{th}} + 2n_{\text{det}}) , \quad (\text{S74})$$

where $n_{\text{det}} = (1-\eta)/2\eta$ represents the added noise due to imperfect homodyne detection expressed in an equivalent amount of thermal phonons. Figure 3 of the main text compares Eq. (S74) with the corresponding sensitivities for direct position detection and a backaction evading measurement. OMIT readout surpasses the SQL of position detection for $\eta \geq 0.5$. Since homodyne detection efficiencies $\eta \gtrsim 0.7$ have already been demonstrated experimentally [59], sensitivities beyond the SQL of position detection are feasible with state-of-the-art technology.

VIII. DIFFERENCE TO OPTICAL SUPERCONDUCTING QUBIT READOUT USING MICROWAVE-TO-OPTICAL TRANSDUCTION

In this section, we comment on the differences between our OMIT-based spin readout and a recently demonstrated optical readout of a superconducting qubit using microwave-to-optical transduction [35]. In this impressive experiment, Delaney *et al.* couple a superconducting transmon qubit dispersively to a microwave cavity, which is optomechanically coupled to a mechanical mode of a silicon-nitride membrane. In addition, the mechanical mode is optomechanically coupled to an optical cavity, such that microwave-to-optical transduction can be achieved by applying simultaneous microwave and optical drives that are red-detuned from the respective cavity resonance frequencies by a mechanical frequency. The qubit is read out by sending a microwave pulse into the microwave cavity and transducing the reflected pulse (whose phase quadrature contains information on the qubit's state) into an optical output pulse. This setup requires simultaneous optimization of the microwave-to-mechanical and optical-to-mechanical coupling, which is technically challenging but can be achieved by spatially separating the interaction regions with the microwave and optical modes on the membrane.

In our scheme, we eliminated the intermediary microwave mode by directly coupling the spins to the mechanical mode. This reduces experimental complexity since simultaneous optimization of two different optomechanical couplings is no longer required. Moreover, Delaney *et al.* probe the qubit by applying a microwave pulse, which would correspond to a mechanical drive in our setup. We do not need this separate mechanical drive since the optical probe laser acts as a mechanical drive, which gives rise to a convenient *all-optical* readout protocol. Finally, unlike in superconducting qubits, the microwave coupling of single solid-state spins is tiny, which precludes using Delaney *et al.*'s readout scheme in a solid-state platform.